

The Spatial Distribution of Satellite Galaxies

Ingólfur Ágústsson^{1*} and Tereasa G. Brainerd¹

¹*Boston University, Department of Astronomy, 725 Commonwealth Ave., Boston, MA, USA, 02215*

27 October 2011

ABSTRACT

We use the first Millennium Run simulation (MRS) to investigate the spatial locations of the satellites of relatively isolated host galaxies. The stellar masses of the MRS hosts span a range of $10.3 \leq \log_{10} [M_*/M_\odot] \leq 11.5$, and host-satellite systems were selected via typical redshift space proximity criteria. The 3-D locations of the MRS satellites are well-fitted by a combination of a Navarro, Frenk and White (NFW) density profile and a power law distribution. At fixed host stellar mass, the NFW scale parameter, r_s , for the satellites of red MRS host galaxies exceeds that for the satellites of blue MRS host galaxies. In both cases the dependence of r_s on host stellar mass is well-fitted by a power law. For the satellites of red MRS hosts, $r_s^{\text{red}} \propto (M_*/M_\odot)^{0.71 \pm 0.05}$, while for the satellites of blue MRS hosts, $r_s^{\text{blue}} \propto (M_*/M_\odot)^{0.48 \pm 0.07}$. We perform model fits to the 2-D (i.e., projected) locations of the MRS satellites from which we find that, with the exception of the satellites of the most massive red MRS hosts, the 2-D analysis accurately recovers the values of r_s that were found using the full 3-D analysis. Finally, we investigate the locations of the satellites of relatively isolated host galaxies in the seventh data release of the Sloan Digital Sky Survey (SDSS). The SDSS hosts have stellar masses in the range $10.6 \leq \log_{10} [M_*/M_\odot] \leq 11.2$, and the host-satellite systems were selected using the same criteria that were used for the MRS. The locations of the SDSS satellites are well-fitted by the NFW and power law model, but due to the small size of the SDSS sample and the fact that few SDSS satellites are found within projected radii $R_p \leq 75$ kpc of their hosts, the error bounds on r_s are large. There is, however, a weak indication that the values of r_s for the satellites of the red SDSS hosts exceeds that of the satellites of the blue SDSS hosts: $r_s^{\text{red}} = 122 \pm 40$ kpc and $r_s^{\text{blue}} = 38 \pm 29$ kpc.

Key words: methods: statistical – galaxies: dwarf – galaxies: fundamental parameters – galaxies: haloes – galaxies: structure – dark matter

1 INTRODUCTION

The spatial distributions of small, faint satellite galaxies have the potential to place strong constraints on the nature of the dark matter haloes surrounding the large, bright “host” galaxies about which the satellites orbit. Recent observational studies of the projected locations (i.e., the angular distribution) of the satellites of relatively isolated host galaxies have shown that, when the satellite locations are averaged over all satellites in the sample, the satellites are found preferentially close to the major axes of their hosts (e.g., Sales & Lambas 2004, 2009; Brainerd 2005; Azzaro et al. 2007; Ágústsson & Brainerd 2010, hereafter AB10; Ágústsson & Brainerd 2011). In addition, the projected locations of the satellites of relatively isolated host galaxies depend upon various physical properties of the hosts themselves (e.g. Azzaro et al. 2007; AB10; Siverd et al. 2009). The locations of the satellites of the host galaxies with the reddest colours and largest stellar masses are highly-anisotropic, and the satellites are found close to the major axes of their hosts. The locations of the satellites of the host galaxies with the bluest colours and lowest stellar masses, however, show little to no anisotropy. The relatively isolated host galaxies typically have stellar masses in the range $10^{10} M_{\text{sun}}$ to $10^{12} M_{\text{sun}}$ and, hence, their morphologies are likely to be “regular” (e.g., elliptical, spiral or lenticular). Therefore, the trend of observed satellite locations with the physical properties of the hosts is effectively a trend with host galaxy morphology since the reddest hosts are predominately ellipticals while the bluest hosts are predominately spirals.

Using very simple assumptions about the ways in which luminous host galaxies might be embedded within their dark matter haloes, Ágústsson & Brainerd (2006) and AB10 showed that the observed locations of satellite galaxies can be easily reproduced from simulations of Λ -dominated Cold Dark Matter (CDM) universes. In particular AB10 showed that the observed trends of projected satellite locations with host colour and host stellar mass can only be reproduced if elliptical and non-elliptical (i.e., “disk”) hosts are embedded within their haloes in different ways. Specifically, AB10 found that mass and light must be well-aligned in elliptical hosts, resulting from a model in which ellipticals are essentially miniature versions of their dark matter haloes. In the case of the disk hosts, AB10 found that mass

* E-mail: ingolfur@bu.edu (IA); brainerd@bu.edu (TGB)

and light are poorly aligned, resulting from a model in which the angular momentum of the host’s disk is aligned with the angular momentum of its dark matter halo. Since the halo angular momentum vectors are not aligned with any of the halo principle axes (e.g., Bett et al. 2007), misalignment of mass and light in disk hosts therefore occurs.

Here we use the first Millennium Run simulation (MRS; Springel et al. 2005) to investigate the real space (as opposed to redshift space) distribution of satellite galaxies around their hosts. Our work differs from the work of Sales et al. (2007) in that here we select our host and satellite systems in exactly the same way as must be done for an observational sample (i.e., a sample drawn from a large redshift survey), whereas Sales et al. (2007) selected their hosts and satellites using the full 3-D information that is available in the simulation. Of course, such full 3-D information is not generally available for a large observational sample of host galaxies and their satellites (i.e., since the distances to the galaxies are unknown). Here our theoretical sample of hosts and satellites is completely analogous to an observational sample, including the unavoidable presence of false satellites (or “interlopers”) in the data. Therefore, the analysis that we present can be applied directly to observational samples that have been selected in a manner similar to that which we adopt.

Using our theoretical host-satellite sample, we obtain a simple parametrisation for the number density of satellites in 3-D. The model that we adopt allows us to recover the most important parameters of the 3-D satellite distribution when only typical observational data (i.e., the 2-D, projected satellite locations) are used. In addition, we investigate the dependence of the model parameters on physical properties of the host galaxies, including colour and stellar mass. Finally, we apply our model to the observed locations of satellite galaxies in the seventh data release of the Sloan Digital Sky Survey (SDSS; Abazajian et al. 2009; Fukugita et al. 1996; Hogg et al. 2001; Smith et al. 2002; Strauss et al. 2002; York et al. 2000) and we extract the best-fitting model parameters. Here we do not directly address the question as to whether the satellites are fair tracers of the dark matter particles that are found within the hosts’ haloes. We instead leave a discussion of whether or not satellites are biased tracers of the mass distribution to a forthcoming companion paper (Ágústsson & Brainerd 2012).

The outline of the paper is as follows. In §2, we discuss the way in which we select relatively isolated host galaxies and their satellites, and we describe the theoretical and observational samples that we use in our analysis. In §3 we discuss the way in which we create composite hosts by stacking together many host-satellite systems. In §4 we compute

the 3-D and 2-D spatial distributions of the MRS satellites and we determine the best-fit model parameters for the distribution of the MRS satellites as a function of physical properties of the host galaxies. In §5 we compute the 2-D spatial distribution of the SDSS satellite galaxies and we determine best-fit model parameters as a function of the rest-frame colours of the hosts. Finally, in §6 we present a summary and discussion of our results.

2 DATA SETS

Host galaxies and their satellites are selected from large observational surveys via proximity criteria which are implemented in redshift space, not real space. In other words, satellite galaxies are selected to be faint objects that are located “close to” bright objects, both in projected radial distance on the sky, R_p , and in relative line of sight velocity, $|dv|$. Here we use the selection criteria from AB10, which yield a population of relatively isolated host galaxies and their satellites. The individual host galaxies dominate the kinematics of the systems and, for comparison, if the Local Group were viewed by an external observer, the Milky Way and M31 would both be rejected from the sample. Specifically, our selection criteria require that the host galaxies be at least 2.5 times more luminous than any other galaxy that is found within a projected radial distance $R_p \leq 700$ kpc and a relative line of sight velocity $|dv| \leq 1000$ km sec⁻¹. Satellites must be found within a projected radial distance $R_p \leq 500$ kpc of their host and must have a relative line of sight velocity $|dv| \leq 500$ km sec⁻¹. In addition, each satellite must be at least 6.25 times fainter than its host. In order to eliminate a small number of systems that pass the above tests but which are likely to be clusters or groups (i.e., instead of relatively isolated host-satellite systems), we impose two further restrictions: [1] the luminosity of each host must exceed the sum total of the luminosities of its satellites, and [2] each host must have fewer than nine satellites. The choice of the maximum number of satellites is somewhat arbitrary and there is no significant effect on our results if we instead choose a different maximum value of, say, four or five satellites. This is due to the fact that most host galaxies have only one or two satellites (see Figure 1 of AB10), and the inclusion of a handful of systems with many satellites in the analysis does not affect the results in any substantial way.

Our theoretical host-satellite sample is taken directly from AB10, and we refer the reader to AB10 for a detailed discussion of the sample. The hosts and satellites were obtained by implementing the above selection criteria for the all-sky mock redshift survey (Blaižot et al.

2005) of the first Λ CDM Millennium Run simulation (MRS; Springel et al. 2005), resulting in a total of 70,882 hosts and 140,712 satellites. From their B -band bulge-to-disk ratios, $\sim 30\%$ of the MRS host galaxies are classified as ellipticals, while the rest are classified as disk galaxies (either spiral or lenticular). See AB10 and De Lucia et al. (2006) for details of the classification scheme. In addition, we divide our sample of theoretical host galaxies according to their rest-frame optical colours, $(g - r)$, at redshift $z = 0$. To do this, we fit the distributions of the host $(g - r)$ colours by the sum of two Gaussians (e.g., Strateva et al. 2001; Weinmann et al. 2006). In the case of our theoretical host galaxies, the division between the two Gaussians lies at $(g - r) = 0.75$ and, therefore, we define “red” MRS hosts to be those with $(g - r) \geq 0.75$ and “blue” MRS hosts to be those with $(g - r) < 0.75$.

The semi-analytic galaxy formation model that was used to create the mock redshift survey assigns each MRS galaxy one of three possible “types”: type 0, type 1, or type 2 (e.g., De Lucia & Blaizot 2007). Type 0 galaxies are the central galaxies of their friends-of-friends (FOF) haloes, while type 1 galaxies are the central galaxies of “subhaloes”. In other words, type 1 galaxies have their own self-bound dark matter subhalo, which is itself contained within a larger dark matter halo. Type 2 galaxies have been stripped of their dark matter and therefore lack distinct substructure. In our full sample, 94% of the MRS hosts are type 0 objects (i.e., they are the central galaxies of their own FOF haloes). In contrast, the MRS satellites in our full sample are primarily type 1 or type 2 objects (41% and 39% of the full sample, respectively). That is, the majority of the theoretical satellites are contained within a larger dark matter halo, as would be expected for genuine satellites. The remainder of the MRS satellites are type 0 objects and, hence, they are central galaxies of their own FOF haloes. These latter objects are examples of “interlopers” – objects which pass the redshift space proximity tests but which are not physically close to a host galaxy. Without direct knowledge of the distances to all of the galaxies, the presence of interlopers in the samples of host galaxies and their satellites is unavoidable. However, since we select hosts and satellites from the simulation and from the observed universe using identical criteria, the level of interloper contamination should be similar in both the theoretical sample and the observational sample.

Our observational host-satellite sample was obtained from the seventh data release of the Sloan Digital Sky Survey and is nearly identical to the SDSS host-satellite sample of AB10. Like AB10, we obtain the SDSS hosts and their satellites by implementing the above selection criteria using all SDSS objects with high quality redshifts ($z_{\text{conf}} > 0.9$), galaxy-type

spectra (specClass = 2), extinction corrected apparent magnitudes $r \leq 17.77$, and redshifts in the range $0.01 \leq z \leq 0.15$ (see AB10). Also like AB10, we require the images of the SDSS galaxies to be free from obvious aberrations in the imaging (for which we performed a visual check), and the host galaxies must not be located close to a survey edge (i.e., each host must be surrounded by spectroscopic targets from the SDSS, within the area of interest). Unlike AB10, however, here we require that all host galaxies have measured stellar masses, since we will ultimately be using stellar mass to divide our host sample below. Stellar masses for the SDSS hosts, computed using the philosophy of Kauffmann et al. (2003) and Salim et al. (2007) are publicly available at <http://www.mpa-garching.mpg.de/SDSS/>. In addition, instead of the cosmological parameters adopted in AB10, here we use the updated, best-fit cosmological parameters from the seven-year WMAP results ($H_0 = 70.4 \text{ km sec}^{-1} \text{ Mpc}^{-1}$, $\Omega_{\Lambda 0} = 0.727$, and $\Omega_{m0} = 0.273$; Komatsu et al. 2011) when we compute projected radial distances and luminosity ratios in the SDSS. The resulting host-satellite sample consists of 4,266 hosts and 6,821 satellites, which is slightly smaller than the sample of AB10 (4,487 hosts and 7,399 satellites). Approximately 90% of the objects used in AB10 are also contained within the observational host-satellite sample that we use here. As with the theoretical sample above, we fit the sum of two Gaussians to the $(g - r)$ colours of the SDSS hosts (K-corrected to $z = 0$; see AB10) to divide the sample into “red” and “blue” hosts. In the case of the SDSS hosts, the division between the two Gaussians lies at $(g - r) = 0.7$ and, therefore, we define red SDSS hosts to be those with $(g - r) \geq 0.7$ and blue SDSS hosts to be those with $(g - r) < 0.7$.

3 COMPOSITE HOSTS

Due to the bright limiting magnitudes of current redshift surveys, each host galaxy typically has only one or two satellites. Therefore, a single observed host galaxy has too few satellites for reliable constraints to be placed on the dark matter halo of that particular host. However, the large total number of hosts that can be obtained from a modern redshift survey makes it possible to use the satellites as probes of the dark matter haloes of the hosts via ensemble averages. To do this, many host-satellite pairs are stacked together, effectively creating “composite” hosts, each of which have a large number of satellites. In order for such stacking to be reasonable, one has to be fairly certain that the vast majority of the hosts lie at the centres of their haloes. While this may not be the case for galaxies that dominate group

systems (see Skibba et al. 2011 and references therein), we know from AB10 that 94% of the relatively isolated host galaxies in our MRS sample reside at the centres of their haloes. Therefore, stacking of the MRS host galaxies to create composite hosts is well-justified.

When creating the composite hosts, one would ideally stack together hosts whose dark matter haloes have similar masses. Of course, the halo mass is not something that is known for any of the host galaxies in an observational sample, so in practice it is not possible to use halo mass to stack together the hosts in an observational sample. However, the luminosities and stellar masses of simulated galaxies are positively correlated with the masses of their dark matter haloes (e.g., More et al. 2011 and references therein). It should therefore be possible to use either host luminosity or host stellar mass as a proxy for halo mass and to assemble appropriate composite hosts. Shown in the left panel of Figure 1 is the relationship between the halo virial mass (M_{200}) and the r -band absolute magnitude (M_r) for our theoretical host galaxies. Different point types and colours in Figure 1 indicate different morphologies for the host galaxies, as determined from their B -band bulge-to-disk ratios (see AB10). Contours indicate the regions inside which $\sim 95\%$ of the red MRS hosts (orange contours) and $\sim 95\%$ of the blue MRS hosts (purple contours) are found. From the left panel of Figure 1, the spread in the relationship between the halo virial mass and the host luminosity is > 0.3 dex. Therefore, an MRS host with a given luminosity and morphology could have a dark matter halo mass that differs by more than a factor of two from that of another MRS host with the identical luminosity and morphology. Also shown in Figure 1 (right panel) is the relationship between the halo virial mass and the stellar mass for the MRS hosts. The relationship between halo virial mass and stellar mass is much tighter than the relationship between halo virial mass and host luminosity (i.e., the spread is $\lesssim 0.3$ dex). Therefore, it is preferable to use the hosts' stellar masses, rather than their luminosities, when stacking the hosts together. The same conclusion was reached by Sales et al. (2007), who studied satellite galaxies around isolated central galaxies in the MRS.

Since there is a clear bimodal distribution of host galaxy colours (both in the MRS and in the SDSS), we construct our composite hosts by stacking together hosts of a given colour (red or blue) within a given stellar mass range. Figure 2 shows the probability distributions for the stellar masses of the MRS hosts (top panel) and the SDSS hosts (bottom panel). From Figure 2, it is clear that in both cases the hosts with the lowest stellar masses are predominately blue, while the hosts with the highest stellar masses are predominately red. For our purposes we are primarily interested in being able to compare results for host galaxies

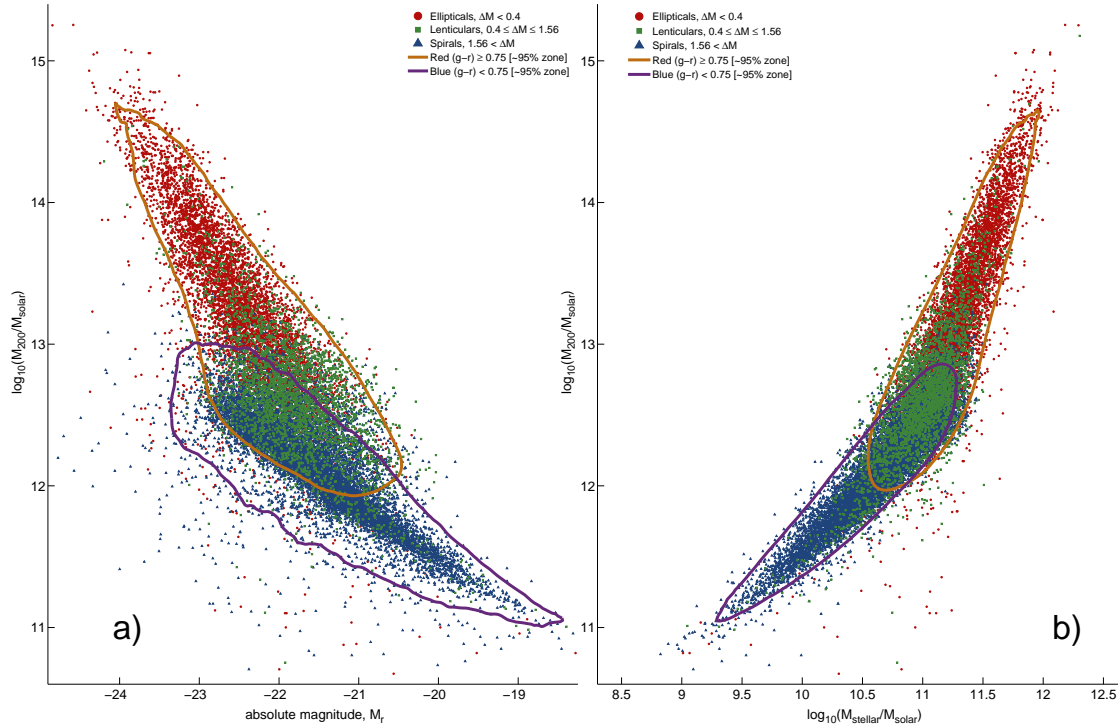


Figure 1. *Left:* Relationship between halo virial mass and r -band absolute magnitude for the MRS host galaxies. *Right:* Relationship between halo virial mass and host stellar mass for the MRS host galaxies. In both panels different point types and colours indicate different host galaxy morphologies (red circles: elliptical, green squares: lenticular, blue triangles: spiral). Contours indicate regions inside which $\sim 95\%$ of the MRS hosts of a given colour are found. See on-line journal for colour figure.

with similar stellar masses, but different colours (i.e., red vs. blue). Therefore, we restrict our analysis below to host galaxies with stellar masses in the range $2 \times 10^{10} \leq M_*/M_\odot \leq 3.2 \times 10^{11}$ (corresponding to $10.3 \leq \log_{10}[M_*/M_\odot] \leq 11.5$), for which there are a significant number of both red and blue galaxies with similar stellar masses (see Figure 2).

To create the composite hosts, we use a fixed bin width of 0.3 dex in stellar mass since the stellar mass estimates for the SDSS galaxies have errors of order ~ 0.3 dex (e.g., Conroy et al. 2009). Given the stellar mass range for the hosts, then, our analysis below will concentrate on composite hosts that reside in one of four stellar mass bins: $10.3 \leq \log_{10}[M_*/M_\odot] < 10.6$ (bin B_1), $10.6 \leq \log_{10}[M_*/M_\odot] < 10.9$ (bin B_2), $10.9 \leq \log_{10}[M_*/M_\odot] < 11.2$ (bin B_3), and $11.2 \leq \log_{10}[M_*/M_\odot] \leq 11.5$ (bin B_4). When referring separately to the red or blue hosts within a given stellar mass bin we will use the notation B_1^{red} , B_1^{blue} , etc.

Tables 1 and 2 show various statistics for our theoretical hosts and satellites in the four stellar mass bins. Table 1 shows the results for red MRS hosts, and Table 2 shows the results for blue MRS hosts. From left to right, the columns list the stellar mass bin, the total number of hosts in the bin, the total number of satellites in the bin, the median host stellar mass for the bin, the mean halo virial radius (r_{200}) for the bin, the mean halo virial mass (M_{200}) for

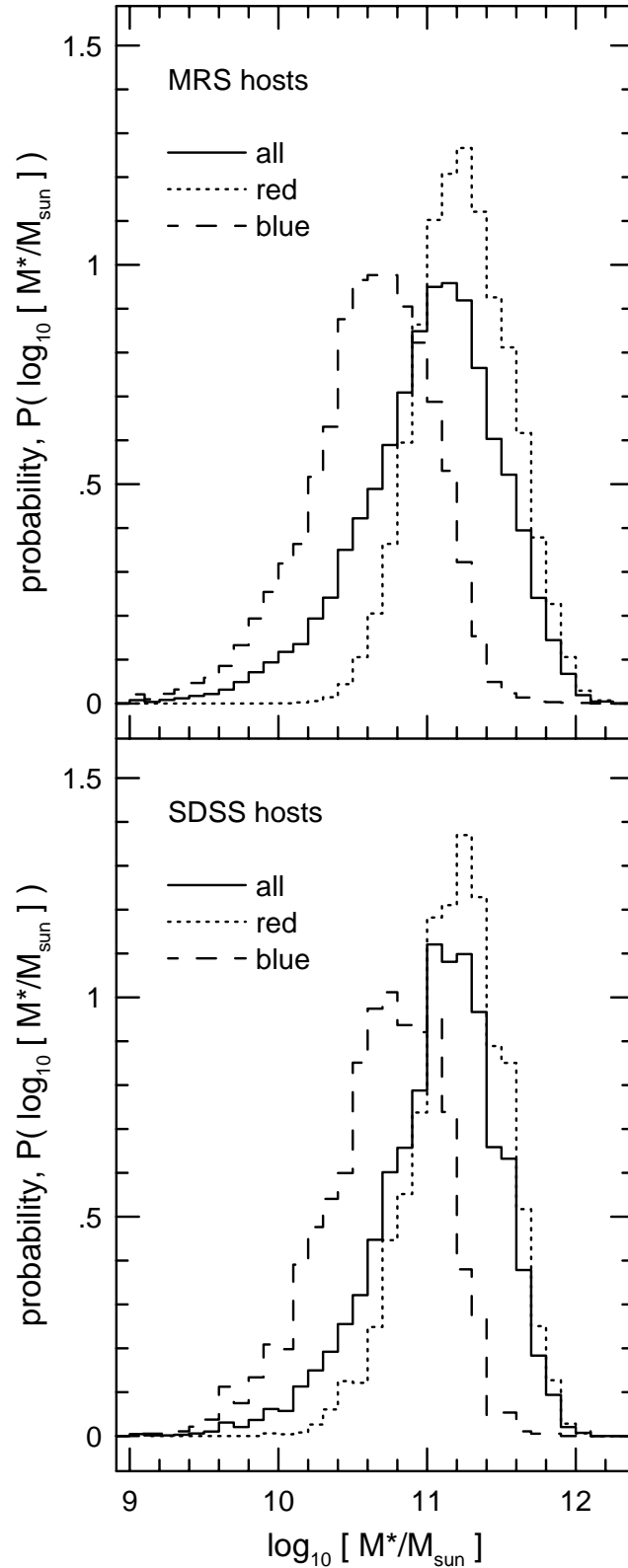


Figure 2. Probability distributions for the stellar masses of the host galaxies. Different line types indicate different sets of hosts (solid lines: all hosts, dotted lines: red hosts, dashed lines: blue hosts). The majority of hosts with high stellar masses have rest-frame optical colours that are red, while the majority of hosts with low stellar masses have rest-frame optical colours that are blue. *Top:* MRS host galaxies. *Bottom:* SDSS host galaxies.

Table 1. Red MRS Host-Satellite Statistics

Bin	N_{host}	N_{sat}	Host $\log_{10} [M_{*,\text{med}}/M_{\odot}]$	Host $\langle r_{200} \rangle$ [kpc]	Host $\langle \log_{10} [M_{200}/M_{\odot}] \rangle$	Host % type 0	Satellite % type 1	Satellite % type 2
B_1^{red}	817	1,348	10.53	218	12.2	91	32	36
B_2^{red}	5,003	9,561	10.80	272	12.5	92	40	37
B_3^{red}	12,244	26,073	11.07	345	12.8	91	45	38
B_4^{red}	10,863	27,220	11.33	500	13.3	90	46	42

Table 2. Blue MRS Host-Satellite Statistics

Bin	N_{host}	N_{sat}	Host $\log_{10} [M_{*,\text{med}}/M_{\odot}]$	Host $\langle r_{200} \rangle$ [kpc]	Host $\langle \log_{10} [M_{200}/M_{\odot}] \rangle$	Host % type 0	Satellite % type 1	Satellite % type 2
B_1^{blue}	7,984	11,831	10.47	190	12.0	98	36	26
B_2^{blue}	8,301	13,675	10.75	231	12.2	97	42	28
B_3^{blue}	5,287	9,765	11.03	283	12.5	96	47	31
B_4^{blue}	1,134	2,511	11.28	367	12.9	96	50	34

the bin, the percentage of hosts that are central galaxies of their own FOF haloes (i.e., type 0), the percentage of satellites that have dark matter substructure surrounding them (i.e., type 1), and the percentage of satellites that have lost all of their dark matter (i.e., type 2). Within a given stellar mass bin, $\sim 20\%$ to 25% of the satellites are, in fact, central galaxies of their own FOF haloes. That is, these satellites are type 0 galaxies in the MRS that are located well outside the actual halo of a host galaxy and are, therefore, interlopers.

Tables 1 and 2 show that the vast majority of the MRS hosts are central galaxies that dominate their own FOF haloes. In the case of these objects, the virial mass is defined to be the mass enclosed within a sphere of mean density $200\rho_c$, centred on the most-bound dark matter particle. Here ρ_c is the critical density for closure of the universe, and r_{200} is the radius of the sphere. In the case of the small number of MRS host galaxies that are type 1 objects, M_{200} is the mass of the subhalo to which they belong and r_{200} is simply calculated from $M_{200} = \frac{800\pi}{3}\rho_c r_{200}^3$.

Despite the similar stellar masses of the red and blue MRS hosts within a given bin, Tables 1 and 2 show that the haloes of the red MRS hosts are generally more massive than those of the blue MRS hosts. Within all of the stellar mass bins, the ratio of the median MRS host stellar masses is $M_{*,\text{med}}^{\text{red}}/M_{*,\text{med}}^{\text{blue}} \lesssim 1.15$, while the ratio of the median host halo virial masses is $M_{200,\text{med}}^{\text{red}}/M_{200,\text{med}}^{\text{blue}} \gtrsim 1.5$. In addition, it is clear from Tables 1 and 2 that each of the stellar mass bins contains MRS hosts with a wide range of halo virial masses (i.e., the scatter between adjacent bins is ~ 0.3 dex), so there is necessarily some overlap between the halo masses within adjacent stellar mass bins.

Figure 3 shows the mean halo mass for the MRS hosts as a function of stellar mass for

the red hosts (top panel) and the blue hosts (bottom panel). Shown for comparison (solid line) is the relationship between mean halo mass and stellar mass for the entire population of galaxies in the two Millennium simulations from Guo et al. (2010), which itself agrees quite well with observational estimates of the halo mass-stellar mass relationship for the galaxy population on average. In the case of the red MRS composite hosts, all but the most massive hosts (bin B_4^{red}) lie on the relationship found by Guo et al. (2010). In the case of the blue MRS composite hosts, it is only the least massive hosts (bins B_1^{blue} and B_2^{blue}) that lie on the relationship found by Guo et al. (2010). It is important to keep in mind that the hosts in our study are not selected to be “average” galaxies; instead they are examples of large, bright galaxies that are relatively isolated within their local regions of space (i.e., the hosts are expected to reside in regions of lower than average density). Figure 3 suggests that the host galaxies in the lower stellar mass bins have dark matter haloes that are similar to those of average galaxies. This is reasonable because, on average, galaxies with low stellar masses tend to be less clustered than galaxies with high stellar masses (e.g., Li et al. 2006).

4 SPATIAL DISTRIBUTION OF SATELLITES IN THE MRS

Full knowledge of the 3-D distribution of galaxies is one of the great luxuries of numerical simulations since, in the observed universe, one is generally restricted to a coordinate system consisting only of the redshifts of the galaxies and their angular locations on the celestial sphere. In this section we use our sample of theoretical satellites from the MRS to investigate the 3-D spatial distribution of the satellites that results when the satellites are selected using redshift space criteria (i.e., exactly as must be done when selecting satellites from a large observational survey). Here we seek an analytic density profile that describes the 3-D distribution of the satellites around their hosts. In addition, we wish to parametrise the density profile in such a way that the parameters can be obtained from the satellite distribution when it is viewed within an observational redshift survey (i.e., where one can only quantify the satellite locations in terms of their projected radial distances from their hosts and their line of sight velocities relative to their hosts).

To begin, let us consider the real space volume within which the satellites are contained. Because of the nature of the redshift space selection criteria (i.e., satellites must be found within a given maximum projected radial distance of their hosts, as well as a given line of sight velocity relative to their hosts), the satellites are effectively found within a cylindrical

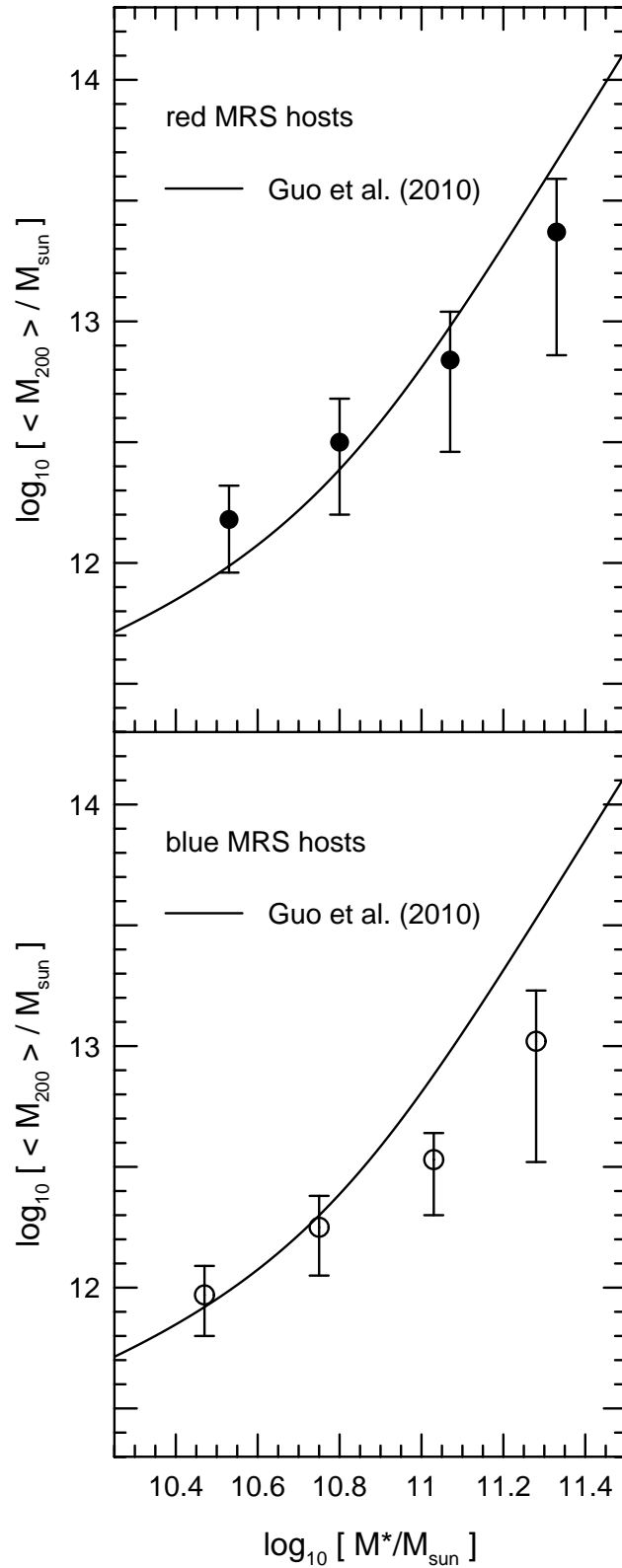


Figure 3. Relationship between host galaxy stellar mass and mean host halo virial mass for the MRS host galaxies. Error bars indicate the 68% confidence limits. Also shown (solid line) is the relationship between stellar mass and halo mass from Guo et al. (2010). *Top:* Red MRS host galaxies. *Bottom:* Blue MRS host galaxies.

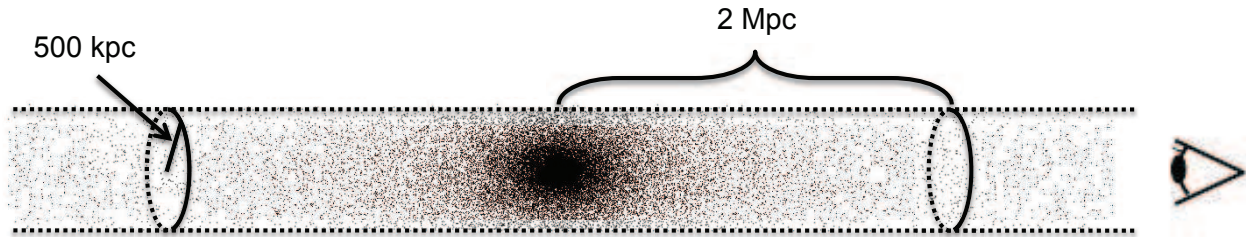


Figure 4. Composite of the real space locations of MRS satellite galaxies from AB10 showing the large-scale cylindrical nature of the selection criteria. Only satellites located within ± 3 Mpc along the line of sight to their hosts are shown. For 3-D distances $r < 500$ kpc, the geometry of the satellite distribution is essentially spherical, while for $r \gg 500$ kpc the satellite distribution is cylindrical. This marked change in geometry causes a discontinuity in the number of satellites as a function of 3-D distance at $r \sim R_{\max} = 500$ kpc (e.g., Figure 6).

volume, where the axis of the cylinder is the line of sight to the host. Technically, the geometry is closer to being a topless cylindrical cone, since the selection criteria make use of angular separations on the sky, as well angular diameter distances that are calculated using the redshifts of the hosts. However, the difference from a cylindrical volume is very small and here we simply adopt the cylindrical geometry (which, for practical purposes, is all that could be done in an observational survey where the actual distances to the galaxies are not known). The cylindrical nature of the selection volume is clear from Figure 4, which shows a composite of the real space locations of the MRS satellite galaxies from AB10. The locations of the satellites are plotted relative to the locations of their hosts. Note that Figure 4 shows only those satellites that are located within ± 3 Mpc of their hosts along the line of sight. The redshift space selection criteria result in the maximum line of sight separation between MRS hosts and satellites in AB10 being ~ 10 Mpc; however, 74% of the satellites are found within 500 kpc of their host along the line of sight, and 84% are found within 1 Mpc (see Figure 5, which shows the distribution of line of sight separations for the MRS hosts and satellites in AB10). From Figures 4 and 5, then, the redshift space selection criteria result in a sample of satellites that, for the most part, are located physically nearby their hosts. However, the tails of the distribution are also very long due to the fact that the redshift space selection criteria cannot distinguish between relative line of sight velocities that are caused by the Hubble flow and those that are caused by the peculiar velocities of satellites moving within the gravitational potentials of their hosts' haloes.

For convenience, we will take the location of the composite host to be the origin of the cylindrical coordinate system in which the satellites are found. We will take the axis of the cylinder to be the line of sight, which in real space corresponds to a coordinate that we label Z . The satellites do not extend to infinite distances along the line of sight. Instead,

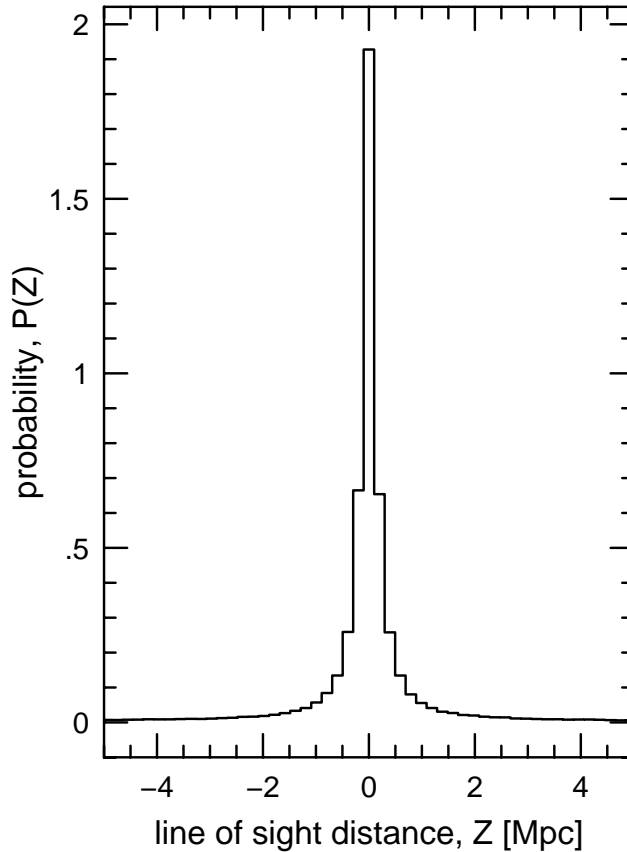


Figure 5. Probability distribution for the line of sight distances between the MRS hosts and satellites from AB10.

they are confined to a cylindrical volume that extends to coordinates $\pm Z_{\max}$ as measured from the composite host. Further, we will take the projected radial distance, R_p , between the hosts and satellites to be the radial coordinate for the cylindrical system. The selection criteria impose a maximum projected radial distance of $R_{\max} \equiv R_{p,\max} = 500$ kpc. For our calculations below we will also impose a formal minimum projected radial distance for the hosts and satellites, $R_{r\min} \equiv R_{p,\min} = 25$ kpc. The reason for this is that we expect to find few satellites in an observational sample with a projected radial distance $R_p \leq 25$ kpc due to the fact that such nearby satellites are generally difficult to distinguish from their hosts in the imaging data.

Figure 6 shows the probability distributions for the 3-D distances between the composite MRS hosts and their satellites. The probability distributions peak at small values of r and they exhibit long tails that actually extend far beyond the maximum values of r that are shown in the figure. Approximately 90% of the MRS satellites are found within a 3-D distance of $r \leq 1$ Mpc from their hosts. Approximately 6% of the MRS satellites are found beyond

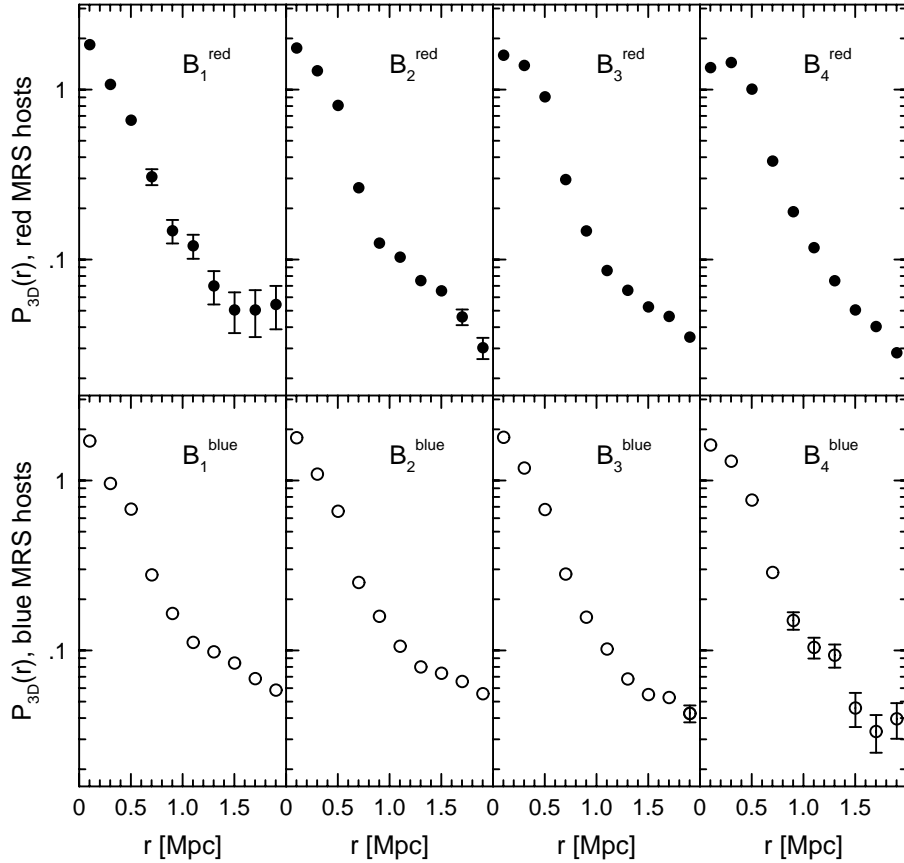


Figure 6. Probability distributions for the 3-D distances between the composite hosts and their satellites. Error bars are omitted when they are comparable to or smaller than the data points. Note that in most cases a discontinuity in the function occurs at $r \sim 500$ kpc, corresponding to the change in geometry from spherical to cylindrical for the satellite locations. (See Figure 4.) *Top*: Red composite hosts. *Bottom*: Blue composite hosts.

a 3-D distance of $r = 3.5$ Mpc from their hosts, and $\lesssim 1\%$ are found as far as 10 Mpc from their hosts. The existence of such long tails in the distributions of the 3-D satellite distances gives rise to a relatively flat distribution of 2-D satellite locations at large projected radii (i.e., due to the fact that, in projection, the distributions have been integrated along the line of sight). The probability distributions for the 2-D satellite locations are shown in Figure 7. In almost all cases, the distribution of the 3-D distances between the hosts and satellites changes markedly at $r \sim R_{\max} = 500$ kpc (i.e., there is a clear discontinuity in the functions at 500 kpc). This marked change is due a manifestation of the overall cylindrical nature of the selection criteria. For 3-D distances $r \leq R_{\max}$, the selection criteria collect essentially all of the satellites within a sphere of radius R_{\max} . For 3-D distances $r > R_{\max}$, the selection criteria only select satellites that are found within a projected radial distance $R_p \leq R_{\max}$. It is, therefore, at 3-D distances of $r \sim R_{\max}$ that the distribution of satellite locations changes from being essentially spherical to being manifestly cylindrical (see Figure 4). Below we

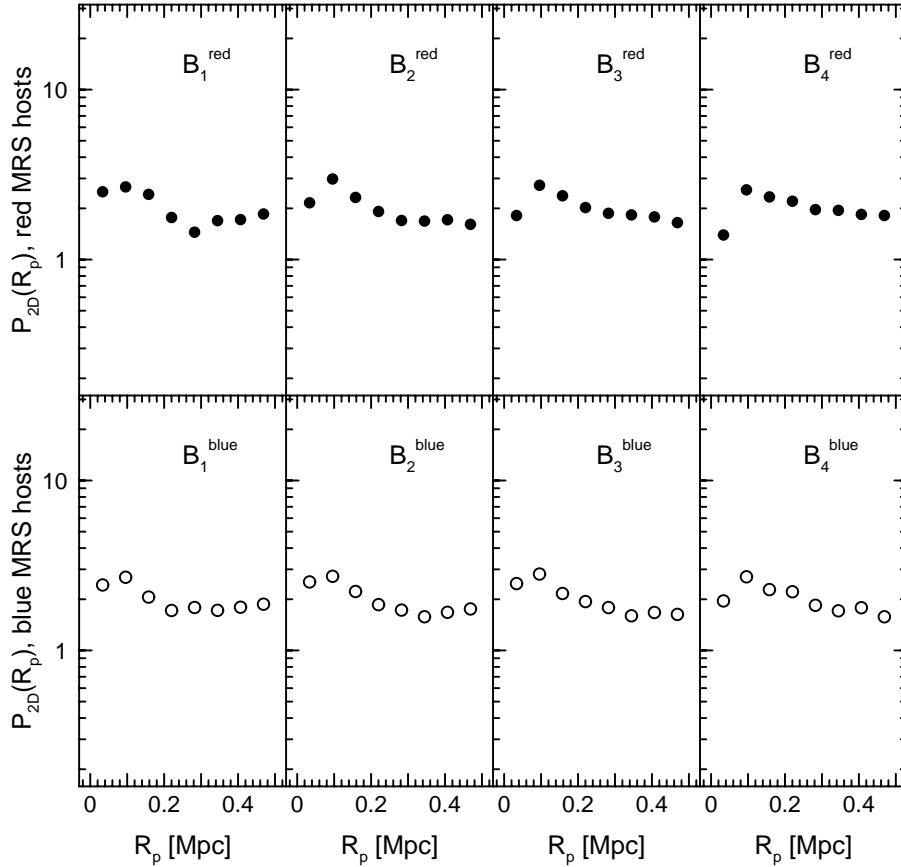


Figure 7. Probability distributions for the projected (2-D) distances between the composite hosts and their satellites. Error bars are omitted since they are comparable to or smaller than the data points. *Top:* Red composite hosts. *Bottom:* Blue composite hosts.

will explicitly account for this change in geometry when we model the number density of satellites as a function of their distances from the hosts.

4.1 3-D Number Density

We will denote the 3-D number density profile of the satellites by $\nu(r)$. The differential satellite number count is then simply the number of satellites that are found within the infinitesimal interval $[r, r + dr]$,

$$dN(r) = \int_S \nu(r) dS dr . \quad (1)$$

Here S is the area of the spherical surface at radius r that is contained within a cylinder of radius R_{\max} . When $r \leq R_{\max}$, the surface S covers the entire sphere (i.e., an area of $4\pi r^2$). For $r > R_{\max}$ the surface S covers two spherical caps, where each cap has a base of radius R_{\max} and height $r - \sqrt{r^2 - R_{\max}^2}$. The surface area of a spherical cap is equal to the area of a circle whose radius equals the distance between the vertex and the base of the cap. Therefore,

for $r > R_{\max}$ we have that the surface area, S , is given by $2\pi \left[R_{\max}^2 + \left(r - \sqrt{r^2 - R_{\max}^2} \right)^2 \right] = 4\pi \left(r^2 - r\sqrt{r^2 - R_{\max}^2} \right)$, where the factor of two accounts for the presence of both spherical caps. We then have

$$dN(r) = \begin{cases} 4\pi r^2 \nu(r) dr, & r \leq R_{\max} \\ 4\pi \left(r^2 - r\sqrt{r^2 - R_{\max}^2} \right) \nu(r) dr, & r > R_{\max}. \end{cases} \quad (2)$$

Equivalently, we can write the differential number count as a single mathematical expression,

$$dN(r) = 4\pi \left[r^2 - r\sqrt{\mathcal{R}(r^2 - R_{\max}^2)} \right] \nu(r) dr, \quad (3)$$

where $\mathcal{R}(x)$ is the ramp function: $\mathcal{R}(x) = x$ for $x \geq 0$ and $\mathcal{R}(x) = 0$ otherwise. Finally, the interior number count is simply the cumulative number of satellites that are enclosed within a 3-D distance r ,

$$N(< r) = \int_0^r dN(r). \quad (4)$$

Based upon previous work, we can anticipate the form of $\nu(r)$ for the MRS satellites. First, we know that the selection criteria yield a sample of objects that consists both genuine satellites and interlopers (see, e.g., AB10 and references therein). Sales et al. (2007) studied the locations of the genuine satellites of isolated galaxies in the MRS, where the satellites were selected using their 3-D locations, not redshift space criteria. From their work, Sales et al. (2007) found that the number density of the genuine satellites was well-fitted by a Navarro, Frenk and White (NFW; Navarro, Frenk & White 1995, 1996, 1997) profile. Therefore, in our host-satellite sample we would expect that for small values of the 3-D host-satellite distance, $\nu(r) \propto (r/r_s)^{-1}(1+r/r_s)^{-2}$, where r_s is the NFW scale radius. However, for very large values of r , we would expect that the hosts and satellites in our sample are not kinematically related (i.e., for very large values of r the ‘‘satellites’’ are actually interlopers) and, so, the form of the probability density for the separation between hosts and satellites should be the same as the probability density for the separation between galaxies as a whole, which is approximated well by a power law. For large values of r , then, we would expect $\nu(r) \propto r^{-\gamma}$.

For simplicity we will adopt a functional form for the number density of satellites that consists of a superposition of an untruncated NFW profile and a power law:

$$\nu(r) \equiv \frac{A}{r/r_s (1 + r/r_s)^2} + \frac{C}{r^\gamma}, \quad (5)$$

where A and C are constants. Clearly, $\nu(r)$ is a pure NFW profile if $C = 0$ and a pure power law if $A = 0$. So long as $\gamma < 3$, the interior number count will be finite. The above model for the satellite number density describes the combination of two populations of objects that

are observationally indistinguishable: one population has a number density that behaves like an NFW profile and the other has a number density that falls off as some power of the distance. On very large scales, the NFW profile falls off as r^{-3} , so that again as long as $\gamma < 3$, the number density of satellites at large distances from the host galaxy becomes dominated by the interlopers that reside in the tails of the distribution. Throughout the discussion below we will refer to these distant objects as “tail interlopers”. Technically, of course, the NFW profile is only valid within the virial radii of dark matter haloes. For convenience, however, we extend the NFW profile beyond the virial radii of the composite hosts in order to smoothly capture the behavior of $\nu(r)$ at radii that are in between those at which the pure NFW profile and the pure power law separately dominate.

Below we will treat the NFW component of the satellite number counts separately from that of the tail interlopers. To do this, we simply make the definitions $\nu(r)_{\text{NFW}} \equiv A(r/r_s)^{-1}(1+r/r_s)^{-2}$ and $\nu(r)_{\text{tail}} \equiv Cr^{-\gamma}$. Using Equations (3) and (4), the 3-D differential and interior number counts of the satellites in the NFW component are then given by

$$dN_{\text{NFW}}(r) = 4\pi Ar_s \frac{r - \sqrt{\mathcal{R}(r^2 - R_{\text{max}}^2)}}{(1 + r/r_s)^2} dr \quad (6)$$

$$N_{\text{NFW}}(< r) = 4\pi Ar_s^3 \left[\ln(1 + r/r_s) - \frac{r/r_s}{1 + r/r_s} - g_{\text{NFW}}(r) \right], \quad (7)$$

where

$$g_{\text{NFW}}(r) = \begin{cases} 0 & r \leq R_{\text{max}} \\ \cosh^{-1}\left(\frac{r}{R_{\text{max}}}\right) - \frac{\sqrt{r^2 - R_{\text{max}}^2}}{r + r_s} - \frac{r_s \cos^{-1}\left(\frac{rr_s + R_{\text{max}}^2}{(r+r_s)R_{\text{max}}}\right)}{\sqrt{R_{\text{max}}^2 - r_s^2}} & r > R_{\text{max}} \end{cases} \quad (8)$$

The 3-D differential and interior number counts of the tail interlopers are given by

$$dN_{\text{tail}} = 4\pi Cr^{-\gamma} \left[r^2 - r\sqrt{\mathcal{R}(r^2 - R_{\text{max}}^2)} \right] dr \quad (9)$$

$$N_{\text{tail}}(< r) = 4\pi C \left[(3 - \gamma)^{-1} r^{(3-\gamma)} - R_{\text{max}}^{(3-\gamma)} g_{\text{tail}}(r/R_{\text{max}}) \right], \quad (10)$$

where

$$g_{\text{tail}}(x) = \begin{cases} 0 & x \leq 1 \\ \frac{1}{2} \left[x\sqrt{x^2 - 1} - \cosh^{-1}(x) \right] & x > 1, \gamma = 1 \\ \frac{1}{(3-\gamma)(\gamma-1)} \left[\frac{\sqrt{x^2-1}}{x^\gamma} \{(\gamma-1)x^2 + 1\} + \frac{\gamma}{2} B\left(x^{-2}; \frac{\gamma+1}{2}, \frac{1}{2}\right) - \frac{\sqrt{\pi}\Gamma\left(\frac{\gamma+1}{2}\right)}{\Gamma\left(\frac{\gamma}{2}\right)} \right] & x > 1, \gamma \neq 1 \end{cases} \quad (11)$$

Here $B(y; a, b) \equiv \int_0^y t^{a-1} (1-t)^{b-1} dt$ is the incomplete Beta function.

4.2 Projected Number Density

The surface number density of the satellites as a function of projected radial distance, R_p , is simply obtained by integrating the 3-D number density along the line of sight, $\Sigma(R_p) = \int \nu(\sqrt{R_p^2 + Z^2}) dZ$. Since the satellites are confined to a cylinder of length $2Z_{\max}$ (i.e., the line of sight coordinates of the satellites are confined to $|Z| \leq Z_{\max}$, centred on the hosts), the surface number density becomes

$$\Sigma(R_p) = 2 \int_{R_p}^{\sqrt{R_p^2 + Z_{\max}^2}} \frac{\nu(r) r}{\sqrt{r^2 - R_p^2}} dr, \quad (12)$$

where r is the 3-D distance.

As in the previous section, we treat the satellites in the NFW component separately from the tail interlopers. Using $\nu_{\text{NFW}}(r)$ in Equation (12) above, we find that the surface number density of the satellites in the NFW component is given by

$$\Sigma_{\text{NFW}}(R_p) = \frac{2Ar_s}{(R_p/r_s)^2 - 1} \left[\frac{Z_{\max}/r_s}{1 + \sqrt{(R_p/r_s)^2 + (Z_{\max}/r_s)^2}} - \frac{\sin^{-1} \left(\frac{Z_{\max}}{R_p} \frac{\sqrt{(R_p/r_s)^2 - 1}}{1 + \sqrt{(R_p/r_s)^2 + (Z_{\max}/r_s)^2}} \right)}{\sqrt{(R_p/r_s)^2 - 1}} \right] \quad (13)$$

(c.f. Bartelmann 1996). The differential number count for the satellites in the NFW component, as seen in projection on the sky, is then simply $dN_{p,\text{NFW}}(R_p) = 2\pi R_p \Sigma_{\text{NFW}}(R_p) dR_p$. Using Equation (13) above for Σ_{NFW} we then find that the interior number count of satellites in the NFW component, as seen in projection on the sky, is

$$N_{p,\text{NFW}}(< R_p) = 4\pi A r_s^3 \left[\ln \left(1 + \frac{Z_{\max}}{r_s} \right) - \sinh^{-1} \left(\frac{Z_{\max}}{R_p} \right) + \frac{1}{\sqrt{(R_p/r_s)^2 - 1}} \sin^{-1} \left(\frac{Z_{\max}}{R_p} \frac{\sqrt{(R_p/r_s)^2 - 1}}{1 + \sqrt{(R_p/r_s)^2 + (Z_{\max}/r_s)^2}} \right) \right]. \quad (14)$$

Similarly, the differential number count for the tail interlopers, as seen in projection, is given by $dN_{p,\text{tail}}(R_p) = 2\pi R_p \Sigma_{\text{tail}}(R_p) dR_p$, where

$$\Sigma_{\text{tail}}(R_p) = \begin{cases} \frac{2C}{(\gamma-1)R_p^{(\gamma-1)}} \left[\frac{\sqrt{\pi}\Gamma(\frac{\gamma+1}{2})}{\Gamma(\frac{\gamma}{2})} - \frac{Z_{\max} R_p^{(\gamma-1)}}{(R_p^2 + Z_{\max}^2)^{\gamma/2}} - \frac{\gamma}{2} B \left(\frac{R_p^2}{R_p^2 + Z_{\max}^2}; \frac{\gamma+1}{2}, \frac{1}{2} \right) \right] & \gamma \neq 1 \\ 2C \sinh^{-1} \left(\frac{Z_{\max}}{R_p} \right) & \gamma = 1 \\ \frac{2C}{R_p} \cot^{-1} \left(\frac{R_p}{Z_{\max}} \right) & \gamma = 2. \end{cases} \quad (15)$$

The interior number count of the tail interlopers, as seen in projection, is therefore

$$N_{p,\text{tail}}(< R_p) = \begin{cases} 2\pi C \frac{R_p^{(3-\gamma)}}{(3-\gamma)} \left[\frac{\sqrt{\pi}\Gamma(\frac{\gamma-1}{2})}{\Gamma(\frac{\gamma}{2})} - \frac{\gamma}{\gamma-1} B \left(\frac{R_p^2}{R_p^2 + Z_{\max}^2}; \frac{\gamma+1}{2}, \frac{1}{2} \right) \right] + \\ 4\pi C \frac{Z_{\max}}{(3-\gamma)(\gamma-2)} \left[Z_{\max}^{(2-\gamma)} - \frac{(2\gamma-3)R_p^2 + (\gamma-1)Z_{\max}^2}{(\gamma-1)(R_p^2 + Z_{\max}^2)^{\gamma/2}} \right] & \gamma \neq 1, 2 \\ 2\pi C \left[R_p^2 \sinh^{-1} \left(R_p^{-1} Z_{\max} \right) + Z_{\max} \left(\sqrt{R_p^2 + Z_{\max}^2} - Z_{\max} \right) \right] & \gamma = 1 \\ 4\pi C \left[R_p \cot^{-1} \left(R_p Z_{\max}^{-1} \right) + Z_{\max} \ln \left(Z_{\max}^{-1} \sqrt{R_p^2 + Z_{\max}^2} \right) \right] & \gamma = 2. \end{cases} \quad (16)$$

4.3 Model Parameters for the Distribution of MRS Satellites

We next use a Maximum Likelihood (ML) method to obtain the best-fit model parameters (and corresponding errors) for the number density of the MRS satellites. We evaluate the goodness of fit using a combination of the Kolmogorov-Smirnov (KS) statistic and bootstrap resampling (e.g., Babu & Feigelson 2006). Bootstrap resampling is necessary since the default rejection confidence levels from the KS statistic, $(1 - P_{\text{KS}}) \times 100\%$, are not reliable when the parameters of the model are determined from the data (e.g., Lilliefors 1969). Here we use non-parametric bootstrap resampling, in which the bootstrap sample is simply drawn directly from the data. Each bootstrap sample then represents one possible realisation of the hosts and satellites, and throughout we apply the ML fitting procedure separately to each of the different realisations. We compute the goodness of the model fits using the distribution of the deviations of the bootstrapped data from the model, which results in unbiased rejection confidence levels. Throughout, we obtain the bootstrap samples by repeatedly drawing (with replacements) from the host sample. It is important to resample the hosts since the satellites are not all independent (i.e., some satellites belong to the same host). By resampling using the hosts, we insure that an individual bootstrap sample will contain all of the host-satellite pairs for a given host.

In order to implement the ML fitting procedure, we define a probability density function for the 3-D distribution of the MRS satellites of the form

$$P_{3\text{-D}}(r) \equiv (1 - f_{\text{tail}})P_{\text{NFW}}(r) + f_{\text{tail}}P_{\text{tail}}(r) , \quad (17)$$

where $0 \leq f_{\text{tail}} \leq 1$ is the fraction of tail interlopers in the sample. Here $P_{\text{NFW}}(r)$ and $P_{\text{tail}}(r)$ are probability density functions for the NFW component and the tail interlopers, respectively. The individual probability density functions, $P_{\text{NFW}}(r)$ and $P_{\text{tail}}(r)$, are based on the interpretation of the differential number counts of MRS satellites, dN , as the unnormalised probability of finding a satellite within the infinitesimal interval $[r, r + dr]$.

The probability density function has three free parameters from the model: r_s , γ , and f_{tail} . It also has three geometrical parameters, two of which are known from the selection criteria: R_{min} and R_{max} , the minimum and maximum projected distances. The third geometrical parameter, r_{max} , is the length of the tail of the satellite distribution in 3-D which is, of course, not known for an observational sample of hosts and satellites. Figures 8, 9, and 10 show the model parameters r_s , γ , and f_{tail} from the ML fits that were computed by adopting five different values of r_{max} (1, 2, 3.5, 5, and 7 Mpc), which enclose 83%, 90%, 94%, 96%,

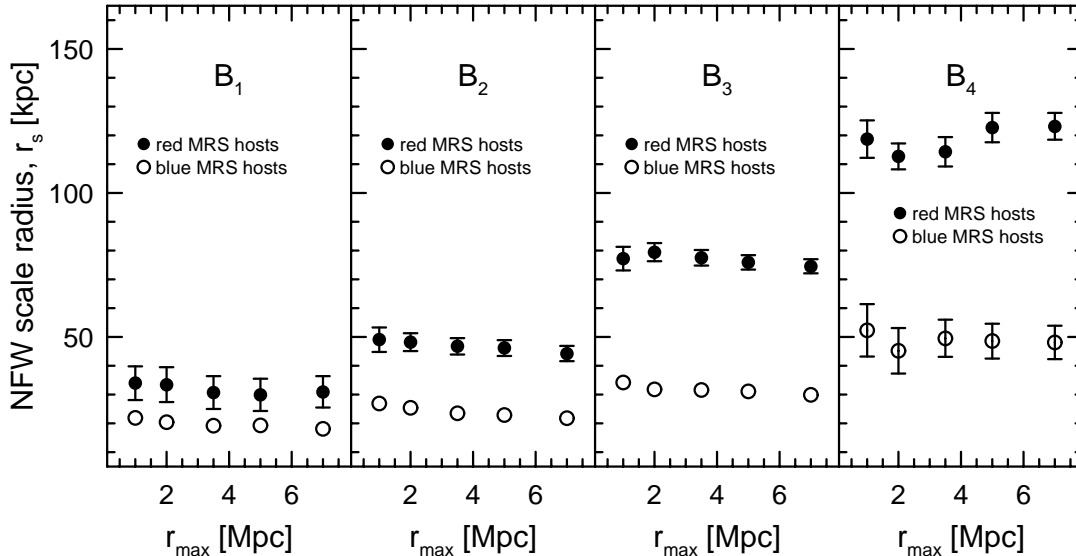


Figure 8. Best-fitting values of the NFW scale parameter, r_s , for the MRS satellites surrounding composite hosts of different stellar masses as a function of r_{\max} . Here a fit to the 3-D satellite locations has been performed. Error bars are omitted when they are comparable to or smaller than the data points. The best-fitting values of r_s are insensitive to the value of r_{\max} that is adopted. Within a given host stellar mass bin, the value of r_s for the satellites of the red composite hosts exceeds that for the satellites of the blue composite hosts.

and 98% of all of the satellites, respectively. From Figure 8, it is clear that r_s increases with increasing host stellar mass, the best-fitting value of r_s is not particularly sensitive to the value of r_{\max} that is adopted and, within a given stellar mass bin, the best-fitting value of r_s is larger for the satellites of red composite hosts than it is for the satellites of blue composite hosts.

With the exception of the satellites of the B_4^{red} composite hosts, the best-fitting value of γ is only weakly-dependent on the value of r_{\max} so long as $r_{\max} \geq 3.5$ Mpc (see Figure 9). In particular, for $r_{\max} = 3.5$ Mpc, $\gamma \simeq 0.8$ for all of the satellites except those of the B_4^{red} composite hosts. Again with the exception of the satellites of the B_4^{red} composite hosts, Figure 10 shows that the value of f_{tail} increases monotonically with r_{\max} , as expected (i.e., as r_{\max} increases we are integrating out to larger and larger distances, where the tail interlopers dominate the sample). The different behaviour of the fits using the satellites of the B_4^{red} hosts is almost certainly connected to our satellite selection criteria. That is, we select only those satellites whose velocities, relative to their hosts, are $|dv| \leq 500$ km sec⁻¹. The B_4^{red} hosts have the most massive haloes (mean virial mass of $\sim 2.3 \times 10^{13} M_{\odot}$) and, hence, the highest velocity dispersions ($\sigma_v \sim 320$ km sec⁻¹). Therefore, it is likely that the sample of satellites around the B_4^{red} hosts is incomplete since our selection criteria only allow for maximum relative velocities that are $\sim 50\%$ greater than the expected velocity dispersion of the hosts’

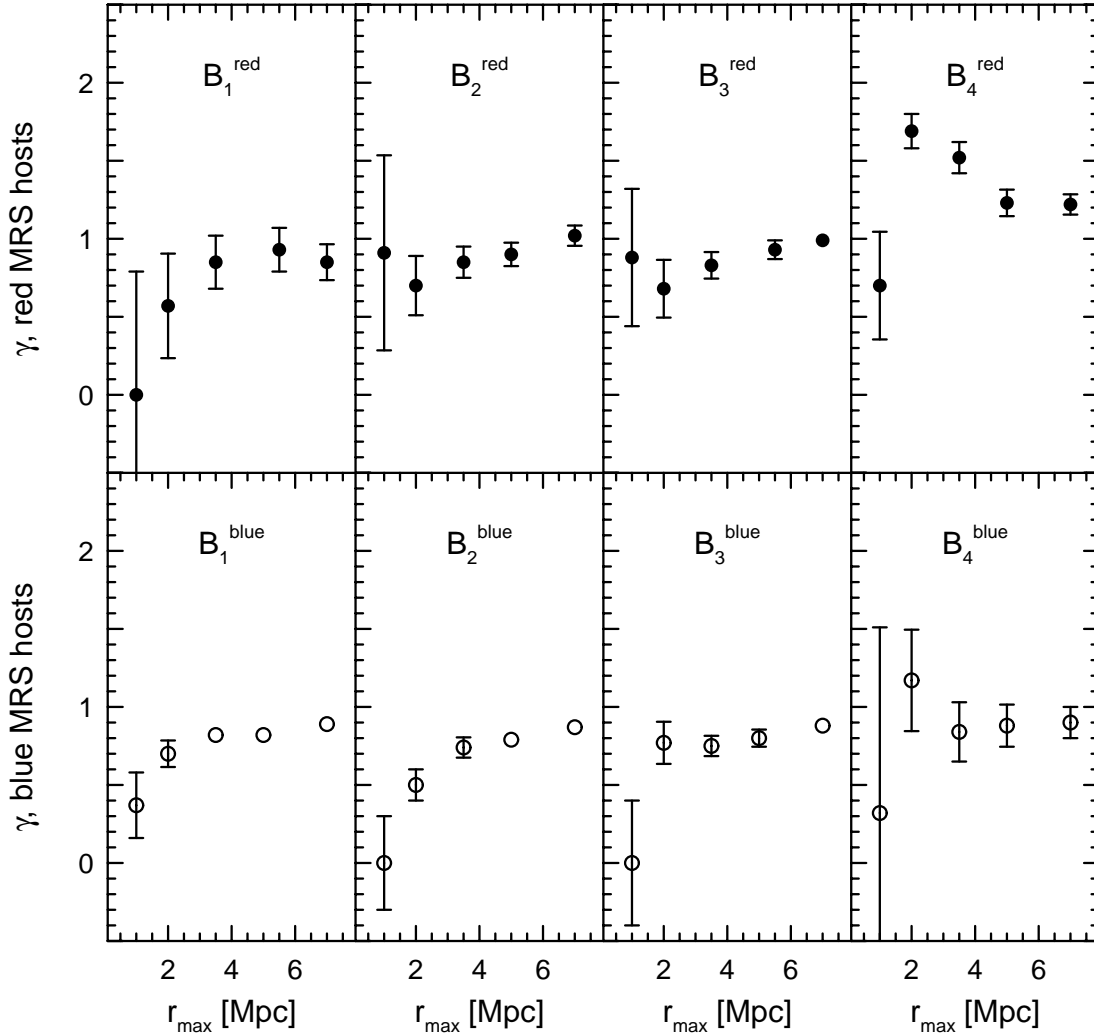


Figure 9. Best-fitting values of the power-law index, γ , for the MRS satellites surrounding composite hosts of different stellar masses as a function of r_{\max} . Here a fit to the 3-D satellite locations has been performed. Error bars are omitted when they are comparable to or smaller than the data points. With the exception of the satellites of the B_4^{red} composite host, for $r_{\max} \geq 3.5$ Mpc the best-fitting values of γ are only weakly-dependent upon the value of r_{\max} .

haloes. In other words, in the case of the B_4^{red} hosts, it is likely that our satellite sample is not fully-representative of the actual satellite distribution around these hosts. From Figure 10, the tail interloper fraction for the satellites of the blue composite hosts always exceeds that for the satellites of the red composite hosts (again with the exception of the satellites around the B_4^{red} hosts). This is expected since there is a strong colour-colour correlation for hosts and their satellites (i.e., the satellites of red hosts tend to be red, while the satellites of blue hosts tend to be blue; Weinmann et al. 2006) and the interloper contamination is known to be considerably larger amongst blue satellites than it is amongst red satellites (e.g., AB10).

We quantify the quality of the model fits that are shown in Figures 8, 9, and 10 by computing the KS statistic, combined with 2,500 bootstrap resamplings. From this, all of

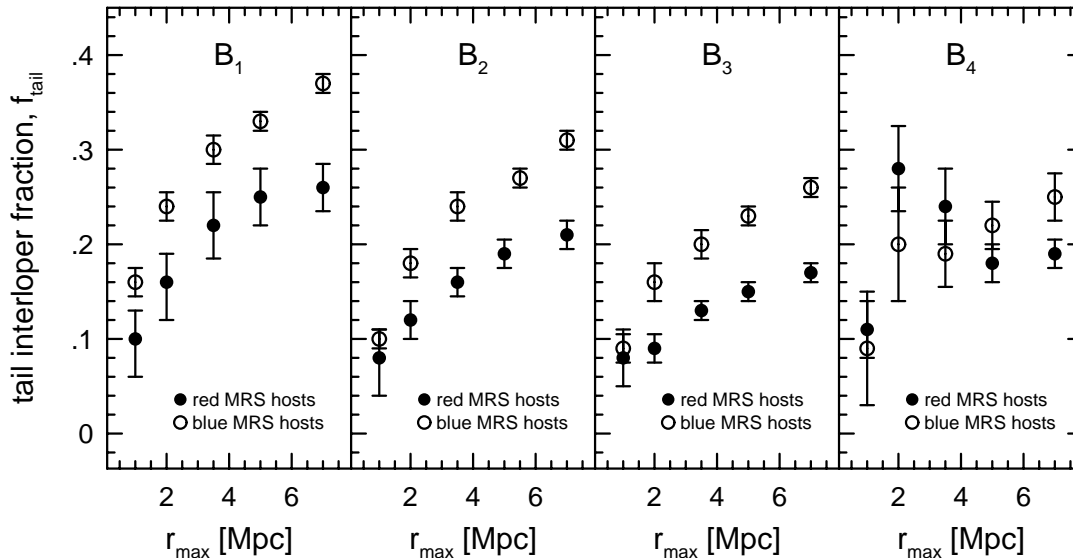


Figure 10. Best-fitting values of the tail interloper fraction, f_{tail} , for the MRS satellites surrounding composite hosts of different stellar masses as a function of r_{max} . Here a fit to the 3-D satellite locations has been performed. With the exception of the satellites of the B_4^{red} composite host, the best-fitting values of f_{tail} increase monotonically with r_{max} , as expected.

the best fitting models shown in Figures 8, 9, and 10 have KS rejection confidence levels of $(1 - P_{\text{KS}}) \times 100\% < 76\%$. That is, in all cases, the fits are satisfactory. In particular, the quality of the fit is unaffected by our choice of the value for r_{max} . We also note that acceptable fits to the 3-D satellite locations require the presence of both the NFW and the tail interloper components. That is, acceptable model fits to the 3-D distribution of the satellites cannot be obtained if we simply set $f_{\text{tail}} = 0$ (i.e., an “NFW-only” model) or $f_{\text{tail}} = 1$ (i.e., a “power-law only” model).

From Figure 8, the 3-D fits to the satellite locations yield best-fitting values of r_s that are insensitive to our choice of r_{max} and, from Figure 9, within the various host stellar mass bins the best-fitting values of γ are nearly identical for $r_{\text{max}} = 3.5$ Mpc (with the exception of the satellites around the B_4^{red} composite hosts). Therefore, in Table 3 we show as examples the values of the KS rejection confidence levels for the 3-D model fits, specifically using $r_{\text{max}} = 3.5$ Mpc. The columns of Table 3 indicate the composite host stellar mass bin, the confidence level at which the model can be rejected when γ is allowed to vary, and the confidence level at which the model can be rejected when γ is fixed at a value of 0.8 (i.e., consistent with the best-fitting value of γ for all but the satellites of the B_4^{red} hosts when we adopt $r_{\text{max}} = 3.5$ Mpc, see Figure 9). From Table 3, then, with the exception of the satellites of the B_4^{red} composite hosts with $\gamma = 0.8$, the KS rejection confidence level is $(1 - P_{\text{KS}}) \times 100\% < 72\%$, indicating good fits. In the case of the satellites of the B_4^{red} hosts,

Table 3. 3-D Model Rejection Confidence Levels, $r_{\max} = 3.5$ Mpc

Bin	$(1 - P_{\text{KS}}) \times 100\%$ unconstrained γ	$(1 - P_{\text{KS}}) \times 100\%$ $\gamma = 0.8$
B_1^{red}	46%	45%
B_2^{red}	3%	4%
B_3^{red}	25%	27%
B_4^{red}	47%	95%
B_1^{blue}	68%	65%
B_2^{blue}	60%	72%
B_3^{blue}	30%	43%
B_4^{blue}	1%	2%

the best-fitting value of the power law index is actually $\gamma = 1.5 \pm 0.1$ for $r_{\max} = 3.5$ Mpc and, hence, when we fix γ to be 0.8, the model is rejected at a modest confidence level (95%; see Table 3).

Figure 11 shows the dependence of the best-fitting values of r_s and f_{tail} on the host stellar mass. From the top panel of Figure 11, the dependence of the NFW scale radius on host stellar mass is well-fitted by a power law, but the index of the power law differs for the red and the blue hosts. Formally, we have $\log_{10} r_s^{\text{red}} = (0.71 \pm 0.05) \log_{10} [M_*/M_\odot] - (6.0 \pm 0.6)$ for the satellites of the red MRS hosts and $\log_{10} r_s^{\text{blue}} = (0.48 \pm 0.07) \log_{10} [M_*/M_\odot] - (3.8 \pm 0.8)$ for the satellites of the blue MRS hosts. From the bottom panel of Figure 11, with the exception of satellites of the B_4^{red} hosts, the tail interloper fraction decreases monotonically with host stellar mass.

Figure 12 shows the values of r_s and f_{tail} that are obtained when we perform fits to the 3-D locations of the satellites and allow the value of γ to vary, versus those that are obtained when we simply fix the value of γ to be 0.8 (i.e., reducing the number of parameters in the model by one). With the exception of the satellites of the B_4^{red} hosts, fixing γ to be 0.8 yields values of r_s and f_{tail} that agree well with the values obtained from the fits in which γ is allowed to vary. Being able to reduce the number of parameters in the model by fixing the value of γ will be useful below when we perform model fits to the projected locations of the satellites (i.e., the 2-D distribution). This is due to the fact that the projected data from an observational sample cannot constrain all of the parameters of the model independently. That is, on large scales both f_{tail} and γ contribute significantly to the shape of the probability distribution for the projected satellite locations, $P_{2\text{-D}}(R_p)$. However, the projected data cannot constrain the value of γ uniquely whilst simultaneously allowing the value of f_{tail} to vary (and vice versa).

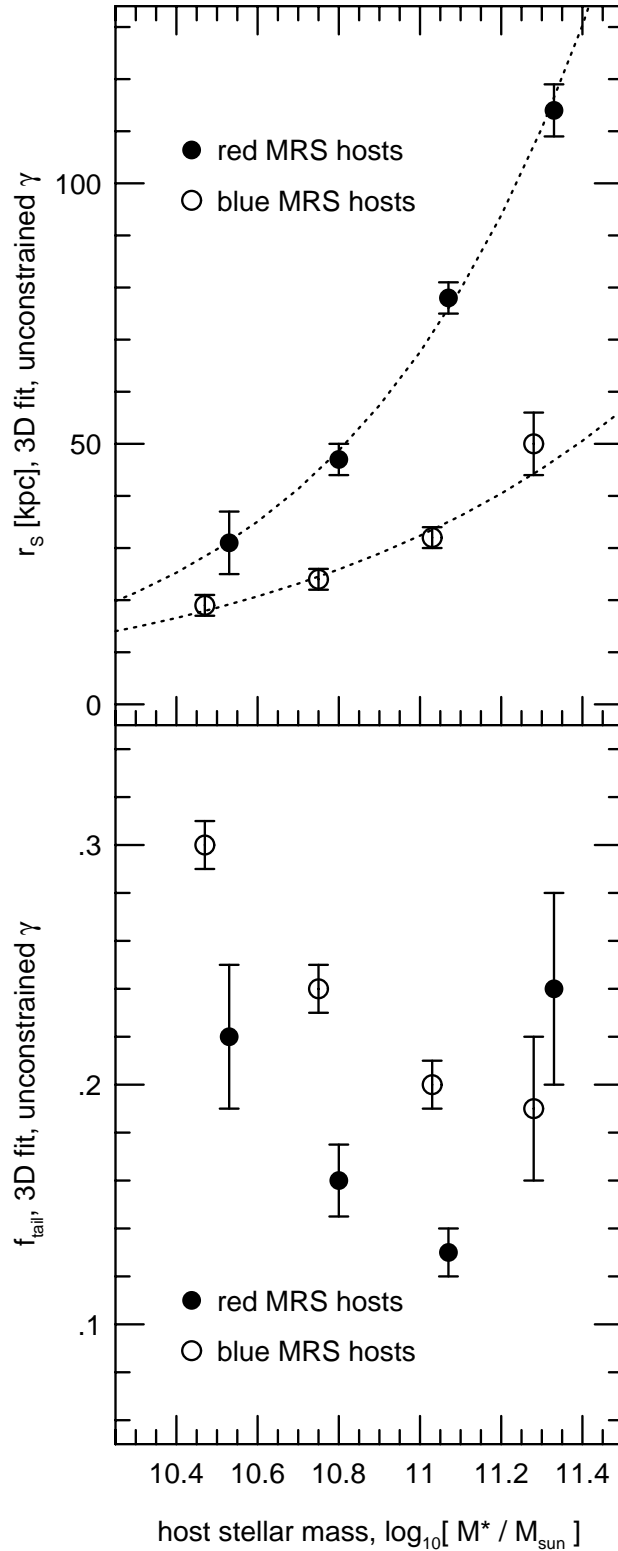


Figure 11. Best-fitting values of the model parameters r_s and f_{tail} as a function of MRS host stellar mass, obtained for $r_{\text{max}} = 3.5$ Mpc. Here fits to the satellite locations in 3-D have been performed and the model parameter γ has been allowed to vary. Different point types correspond to hosts of different colours (solid circles: red MRS hosts; open circles: blue MRS hosts). *Top:* NFW scale parameter, r_s . Dotted lines show the best-fitting power laws for the dependence of r_s on host stellar mass. *Bottom:* Tail interloper fraction, f_{tail} . The value of f_{tail} for the red MRS hosts with the highest stellar masses falls far from the general trend of f_{tail} with host stellar mass. This is likely due to the sample of satellites for these particular hosts being incomplete (see text).

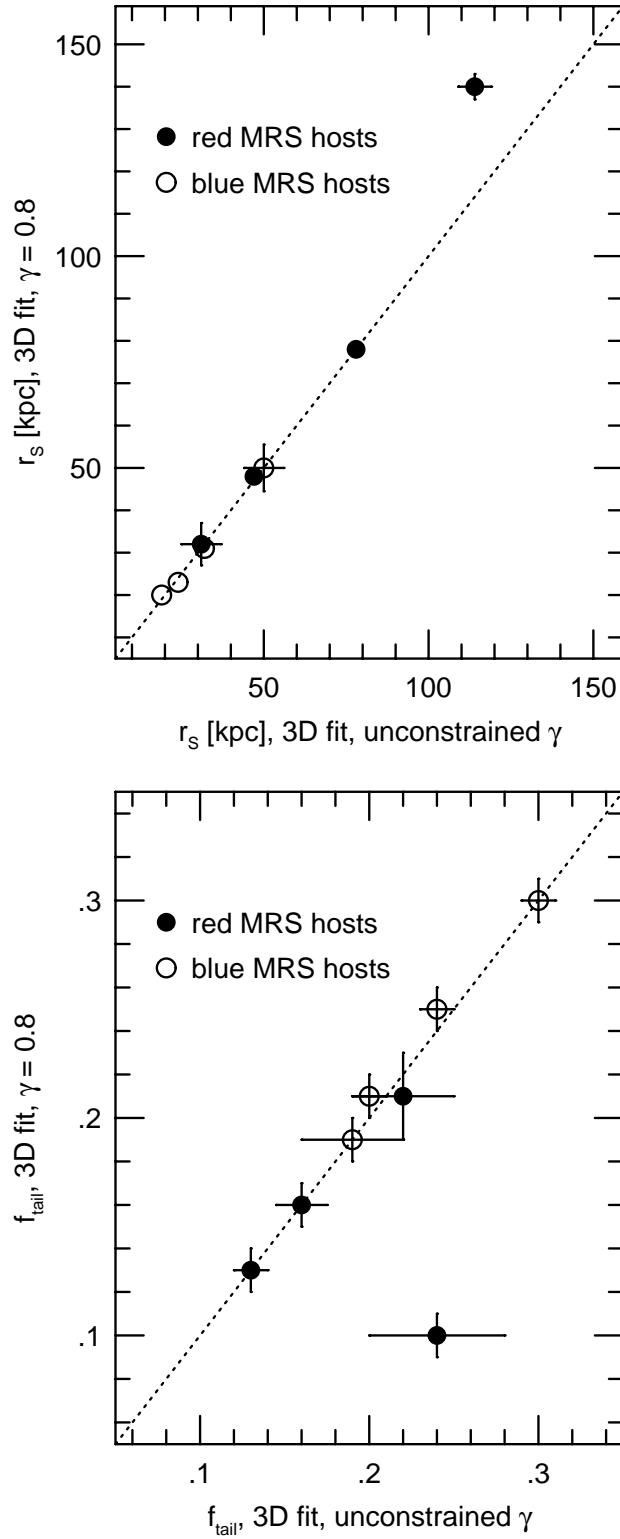


Figure 12. Comparison of best-fitting values of the model parameters r_s and f_{tail} obtained when the parameter γ is allowed to vary (abscissas) and when γ is fixed to a value of 0.8 (ordinates). Here fits to the satellite locations in 3-D have been performed and a value of $r_{\text{max}} = 3.5$ Mpc was adopted. Different point types correspond to hosts of different colours (solid circles: red MRS hosts; open circles: blue MRS hosts). Solid circles that lie away from the general trend correspond to fits to the locations of the satellites of the most massive red MRS hosts, for which $\gamma = 0.8$ is a poor fit (see text). *Top:* NFW scale parameter, r_s . *Bottom:* Tail interloper fraction, f_{tail} .

Table 4. 2-D Model Rejection Confidence Levels, $Z_{\max} = 3.5$ Mpc, $\gamma = 0.8$

Bin	$(1 - P_{\text{KS}}) \times 100\%$
B_1^{red}	6%
B_2^{red}	22%
B_3^{red}	9%
B_4^{red}	28%
B_1^{blue}	27%
B_2^{blue}	5%
B_3^{blue}	1%
B_4^{blue}	1%

In order to obtain best-fitting models to the 2-D locations of the satellites we define a probability density function of the form

$$P_{2\text{-D}}(R_p) \equiv (1 - f_{\text{tail}}) \frac{2\pi R_p \Sigma_{\text{NFW}}(R_p)}{N_{\text{p,NFW}}(<R_{\max}) - N_{\text{p,NFW}}(<R_{\min})} + f_{\text{tail}} \frac{2\pi R_p \Sigma_{\text{tail}}(R_p)}{N_{\text{p,tail}}(<R_{\max}) - N_{\text{p,tail}}(<R_{\min})} . \quad (18)$$

As with the fits to the 3-D satellite locations above, we again implement a ML procedure to find the best-fitting model parameters. We fix γ to be 0.8 and we obtain fits for f_{tail} and r_s from the projected radial locations of the MRS satellites (i.e., here we use all MRS satellites along the line of sight since the physical distances between hosts and satellites are not included in the 2-D data set). Recall that above the values of R_{\min} and R_{\max} for the MRS satellites were chosen to be 25 kpc and 500 kpc, respectively. Taking $Z_{\max} = r_{\max} = 3.5$ Mpc in equations (13)-(16), then, we obtain good model fits and, again with the exception of the satellites of the B_4^{red} hosts, the best-fitting values of r_s from the projected satellite distributions are in good agreement with those obtained from the 3-D distribution. KS rejection confidence levels for the fits to the 2-D satellite distributions are shown in Table 4, and comparisons of the model parameters r_s and f_{tail} obtained from the 2-D and 3-D fits are shown in Figure 13.

From the top panel of Figure 13, we conclude that, except in the case of the satellites of the most massive red hosts (for which our sample is likely incomplete), fitting the projected (2-D) satellite locations with a combination of an NFW component and a power-law component with $\gamma = 0.8$ recovers the values of the NFW scale radius that one would obtain if one knew the full 3-D distribution of the satellites. In the case of the satellites of the B_4^{red} hosts, the two values of r_s disagree at the $\sim 2\sigma$ level ($r_s = 114 \pm 5$ for the 3-D fit and $r_s = 137 \pm 8$ for the 2-D fit). In other words, with the exception of the satellites of the B_4^{red} hosts, Figure 13 suggests that, provided the data sets are sufficiently large, one can

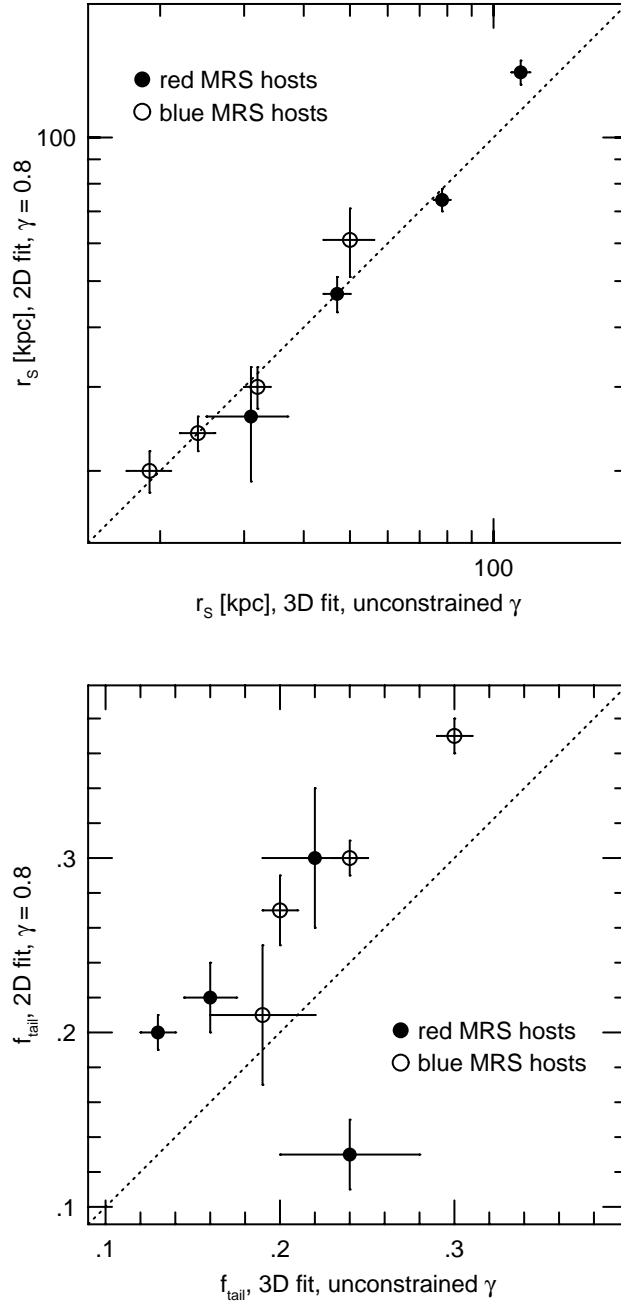


Figure 13. Comparison of best-fitting values of the model parameters r_s and f_{tail} obtained from fits to the 3-D and 2-D (projected) locations of the satellites. Here values of $r_{\text{max}} = Z_{\text{max}} = 3.5$ kpc have been adopted. In the 3-D fits the value of γ is allowed to vary, but in the 2-D fits the value of γ is fixed to 0.8 since γ and f_{tail} cannot be obtained independently of one another. Different point types correspond to hosts of different colours (solid circles: red MRS hosts; open circles: blue MRS hosts). Solid circles that lie away from the general trend correspond to fits to the locations of the satellites of the most massive red MRS hosts, for which $\gamma = 0.8$ is a poor fit (see text). *Top:* NFW scale parameter, r_s . With the exception of the satellites of the B_4^{red} hosts, the values of r_s obtained from the 2-D and 3-D fits agree to within $\sim 1\sigma$. *Bottom:* Tail interloper fraction, f_{tail} . With the exception of the satellites of the B_4^{red} hosts, the values of f_{tail} from the 2-D fits exceed those from the 3-D fits due to the fact that the 2-D fits include all of the satellites, not just those with 3-D distances $r \leq 3.5$ Mpc.

accurately recover the values of r_s from observed host-satellite data sets (i.e., data sets for which the full 3-D satellite distribution is not known).

From the bottom panel of Figure 13, the values of f_{tail} that are obtained with the 2-D fits to the satellite locations generally exceed those obtained with the 3-D fits (the exception again being the satellites of the B_4^{red} hosts). This is due to the fact that in the 3-D fits we used a 3-D maximum distance of $r_{\text{max}} = 3.5$ Mpc and, hence, 6% of the total number of satellites (i.e., those with 3-D distances $r > 3.5$ Mpc) were explicitly excluded from the 3-D fits. In the case of the 2-D fits, however, we must necessarily use all of the satellites along the line of sight since the fits are based solely upon the use of the projected locations of the satellites relative to their hosts. Therefore, we expect f_{tail} to be larger for the 2-D fits than for the 3-D fits simply because of the presence of objects with $r > 3.5$ Mpc in the 2-D data.

5 SPATIAL DISTRIBUTION OF SATELLITES IN THE SDSS

Lastly, we apply the techniques above to the observed locations of the satellites in the SDSS. Here, of course, the locations of the satellites are only known in projection, not in 3-D, so we can only obtain best-fitting model parameters using 2-D data. In addition, the SDSS has far fewer hosts and satellites than does the MRS, which severely impacts our ability to obtain good model fits. There are, in fact, too few SDSS hosts and satellites in each of the individual host stellar mass bins above to perform the calculation. In order to obtain a sufficient number of satellites around both the red and the blue SDSS hosts (i.e., for comparison to each other), we must restrict our analysis to a combination of those hosts whose stellar masses fall within the range $10.6 \leq \log_{10}(M_*/M_\odot) \leq 11.2$. This corresponds to a stellar mass bin of width 0.6 dex (i.e., double the width of the bins used for our analysis of the MRS satellites), and is simply the combination of bins B_2 and B_3 from above.

At small projected separations, R_p , our SDSS host-satellite sample suffers from incompletenesses due to fiber collisions (i.e., the spectra of two galaxies separated by less than 55 arcsec could not be obtained simultaneously; Blanton et al. 2003). Most of the area covered by the SDSS was observed more than once and, therefore, not all galaxies with angular separations < 55 arcsec from their nearest neighbours are missing from the spectroscopic catalogs. However, the incompleteness is sufficiently large that it affects our ability to identify all of the satellites that ought to present in the SDSS sample. The fiber collision scale has a fixed angular separation on the sky and, due to the fact that the hosts are not all

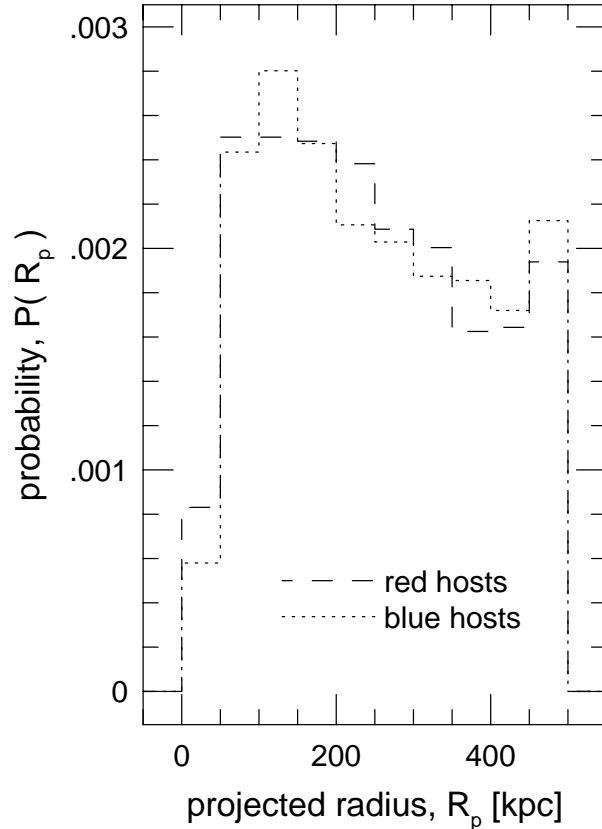


Figure 14. Probability distribution of projected distances, R_p , for the satellites of the B_2 and B_3 SDSS hosts. Few satellites are found at $R_p < 75$ kpc due to the fiber collisions in the SDSS. Dashed line: satellites of red SDSS hosts. Dotted line: satellites of blue SDSS hosts.

located at the same redshift, this translates into different values of projected separation, R_p , inside which fiber collisions may prevent the identification of satellite galaxies.

Figure 14 shows the probability distribution of projected satellite locations, R_p , for all satellites of the B_2 and B_3 SDSS hosts. From this figure, the number of satellites drops significantly for $R_p \leq 75$ kpc. Only 9% of the total number of SDSS satellites are found within projected distances $R_p \leq 75$ kpc. This is due to the fact that for $\sim 85\%$ of the SDSS hosts the fiber collision scale corresponds to a projected distance ≤ 75 kpc. In order to account for the artificial suppression of the satellite number count at small projected distances, then, we further restrict our sample of SDSS objects to those hosts for which the fiber collision scale corresponds to a projected separation $R_p < 75$ kpc (i.e., host with redshifts $z \leq 0.07$). That is, in our analysis below we impose a minimum radius $R_{\min} = 75$ kpc in order to mitigate the effects of the fiber collisions on the host-satellite sample. This final restriction on the data results in a total of 1,201 red SDSS hosts with 1,875 satellites and a total of 657 blue

SDSS hosts with 877 satellites. The median stellar mass of the red SDSS hosts is $1 \times 10^{11} M_{\odot}$ and the median stellar mass of the blue SDSS hosts is $7.3 \times 10^{10} M_{\odot}$.

We obtain best-fitting parameters for the projected locations of the SDSS satellites in the same manner as we did for the projected locations of the MRS satellites, and we fix the values of R_{\min} , R_{\max} , Z_{\max} , and γ to be 75 kpc, 500 kpc, 3.5 Mpc, and 0.8, respectively. We then determine the best-fitting model parameters r_s and f_{tail} using the ML method and compute the KS rejection confidence levels. In the case of the satellites of the red SDSS hosts, we find $r_s^{\text{red}} = 122 \pm 40$ kpc, $f_{\text{tail}}^{\text{red}} = 0.13 \pm 0.10$, and a KS rejection confidence level of $(1 - P_{KS}) \times 100\% = 1\%$ (i.e., a good fit to the model). In the case of the satellites of the blue SDSS hosts, we find $r_s^{\text{blue}} = 38 \pm 29$ kpc, $f_{\text{tail}}^{\text{blue}} = 0.34 \pm 0.09$, and again a KS rejection confidence level of $(1 - P_{KS}) \times 100\% = 1\%$. Although the KS statistic indicates good fits to the models, the NFW scale parameter is not well-constrained in either case. This is most likely due to the fact that we lack SDSS satellites at small values of R_p and, so, the expected peak of the satellite distribution (see Figure 6) is not traced well by the data.

The parameter in which we are most interested is, of course, the NFW scale radius, r_s , and we are especially interested in whether the value of r_s differs for the satellites of red host galaxies and the satellites of blue host galaxies, as we saw above in our analysis of the satellites of MRS host galaxies. That is, from the power law fits to the dependence of r_s on host stellar mass for the red and blue MRS host galaxies, we expect r_s^{red} to exceed r_s^{blue} by a factor of ~ 2.5 . The values of the NFW scale parameters that we obtain for the SDSS satellites are larger than expected based on the values of r_s for the corresponding MRS satellites from the power law fits above (i.e., from the power law fits shown in Figure 11 we expect $r_s^{\text{red}} \simeq 64.6$ kpc and $r_s^{\text{blue}} \simeq 26.0$ kpc for hosts with stellar masses of $1.0 \times 10^{11} M_{\odot}$ and $7.3 \times 10^{10} M_{\odot}$ respectively). In addition, since the values of r_s are so poorly constrained, the difference between r_s^{red} and r_s^{blue} for the SDSS satellites is significant at a level of only $\sim 1.7\sigma$. This is by no means definitive, but it may suggest that the NFW scale parameter for the satellites of red SDSS hosts exceeds that for the satellites of blue SDSS hosts. A definitive measurement of any difference in the values of r_s for the observed satellites of red and blue host galaxies will require larger sample sizes, including samples for which the satellite distribution at small projected radii ($25 \text{ kpc} \lesssim R_p \lesssim 75 \text{ kpc}$) is considerably more complete than it is in our current SDSS sample.

6 DISCUSSION

We have investigated the spatial locations of the satellites of relatively isolated “host” galaxies using a large sample of host galaxies and their satellites that were selected from the first Millennium Run simulation (MRS) using a common set of redshift space selection criteria. Selecting the satellites via redshift criteria results in a geometry for the locations of the satellites, relative to their hosts, that is essentially spherical for small physical separations and is cylindrical for large physical separations. The distinct change in geometry that occurs for the satellite locations at large distances from their hosts is accounted for explicitly in our model for the satellite locations.

The 3-D locations of the MRS satellites are well-fitted by a combination of an NFW profile and a power law. The NFW profile characterises the genuine satellites, while the power law characterises the interlopers (or “false” satellites). It can be shown straightforwardly that the two-component model that we have adopted above is actually a simplification of a triple power law of the form

$$\nu(r) \equiv A \frac{1 + (r/r_t)^{3-\gamma}}{r/r_s(1 + r/r_s)^2} = \frac{A}{r/r_s(1 + r/r_s)^2} + A \left(\frac{r_s}{r_t}\right)^3 \frac{r^2}{(r + r_s)^2} \frac{r_t^\gamma}{r^\gamma} \quad (19)$$

(Ágústsson 2011). Here r_t is a “tail radius” that characterises the transition from the NFW regime of the satellite number density distribution to the tail interloper regime. Although all of the analysis that we have presented here can be reproduced through the use of a triple power law, the expressions for the projected satellite number density that one obtains when using a triple power law are not analytic, unlike the expressions that we show above. Therefore, numerical integrations must be performed and the amount of computing time that is needed in order to complete the bootstrap resamplings is greatly increased.

When using the 3-D locations of the MRS satellites we find that the best-fitting values of the NFW scale radius, r_s , are insensitive to the maximum distance, r_{\max} , that we adopt in our Maximum Likelihood analysis. With the exception of the satellites of the most massive red MRS hosts (for which the satellite sample is likely to be incomplete), the best-fitting power law index, γ , is also largely insensitive to the value of r_{\max} that is adopted, provided $r_{\max} \geq 3.5$ Mpc (i.e., we need a sufficient number of interlopers to be present in the tail of the distribution for the fit to converge to a single value of γ). From the 3-d locations of the MRS satellites, the best-fitting values of the NFW scale radius are functions of both the stellar masses and the rest-frame colours of the host galaxies. At fixed host stellar mass, the values of r_s for the satellites of red MRS hosts exceed those for the satellites of blue MRS

hosts. The dependence of r_s on host stellar mass is well-fitted by a power law, but the index of the power law differs for the satellites of the red vs. blue hosts: $r_s^{\text{red}} \propto (M_*/M_\odot)^{0.71 \pm 0.05}$ and $r_s^{\text{blue}} \propto (M_*/M_\odot)^{0.48 \pm 0.07}$.

When using the 2-D locations of the MRS satellites (i.e., their projected locations relative to their hosts) we find that, again with the exception of the satellites of the most massive red MRS hosts, we can accurately recover the best-fitting values of the NFW scale radius that we obtained when using the full 3-D data. If the mass of the universe is dominated by Cold Dark Matter, then, we expect that the locations of observed satellites in the universe should be well-fitted by a combination of an NFW profile and a power law, and an analysis of a sufficiently large observational sample (for which the satellite locations are known only in projection) will lead to best-fitting values of r_s that will agree with the values that one would obtain if one had full 3-D information for the locations of the observed satellites.

Using the 2-D locations of the satellites of SDSS host galaxies we find that the combination of an NFW profile and a power law provides a good fit to the observed satellite locations. However, due to the fact that the size of the SDSS host-satellite sample is small and very few SDSS satellites are found at projected distances $R_P \leq 75$ kpc, the error bounds on the best-fitting values of the NFW scale radii are large: $r_s^{\text{red}} = 122 \pm 40$ kpc for the satellites of red SDSS hosts and $r_s^{\text{blue}} = 38 \pm 29$ kpc for the satellites of blue SDSS hosts. While not definitive, the values we obtain for r_s^{red} and r_s^{blue} suggest that the NFW scale radius for the satellites of red SDSS hosts exceeds that for the satellites of blues SDSS hosts at a level that is comparable to what we expect from our analysis of the host-satellite systems in the MRS. A definitive determination of the dependence of r_s on the colours of observed host galaxies will require substantially larger samples than can be obtained from the SDSS, including a much greater number of host-satellite pairs in which the satellite is located at a small projected distance ($R_P \leq 75$ kpc) so that the peak of the satellite number density distribution is traced more accurately than it is in the SDSS.

ACKNOWLEDGMENTS

Support from the National Science Foundation under NSF contract AST-0708468 is gratefully acknowledged. Funding for the SDSS and SDSS-II was provided by the Alfred P. Sloan Foundation, the Participating Institutions, the National Science Foundation, the U.S. Department of Energy, the National Aeronautics and Space Administration, the Japanese

Monbukagakusho, the Max Planck Society, and the Higher Education Funding Council for England. The SDSS was managed by the Astrophysical Research Consortium for the Participating Institutions (Univ. of Chicago, Fermilab, the Institute for Advanced Study, the Japan Participation Group, Johns Hopkins Univ., Los Alamos National Laboratory, the Max-Planck-Institute for Astronomy, the Max-Planck-Institute for Astrophysics, New Mexico State Univ., Univ. of Pittsburgh, Princeton Univ., the US Naval Observatory, and Univ. of Washington). The SDSS Web site is <http://www.sdss.org/>.

REFERENCES

- Abazajian, K. et al. 2009, *ApJS*, 182, 543
- Ágústsson, I. 2011, PhD thesis, Boston University
- Ágústsson, I. & Brainerd T. G., 2006, *ApJ*, 650, 550
- Ágústsson, I. & Brainerd T. G., 2010, *ApJ*, 709, 1321
- Ágústsson, I. & Brainerd, T. G., 2011, *ISRN Astronomy & Astrophysics*, vol. 2011, id # 958973 (doi: 10.5402/2011/958973)
- Ágústsson, I. & Brainerd, T. G., 2012, in preparation
- Azzaro, M., Patiri, S. G., Prada, F., & Zentner, A. R. 2007, *MNRAS*, 376, L43
- Babu, G. J. & Feigelson, E. D. 2006, in *ASP Conf. Series. vol. 351, Astronomical Data Analysis Software and Systems XV*, eds. C. Gabriel, C. Arviset, D. Ponz & S. Enrique, 127
- Bartelmann, M. 1996, *AA*, 313, 697
- Bett, P., Eke, V., Frenk, C. S., Jenkins, A., Helly, J. & Navarro, J. 2007 *MNRAS*, 376, 215
- Blaizot, J., Wadadekar, Y., Guiderdoni, B., Colombi, S. T., Bertin, E., Bouchet, F. R., Devriendt, J. E. G., & Hatton, S. 2005, *MNRAS*, 360, 159
- Blanton, M. R., Lin H., Lupton, R. H., Maley, F. M., Young, N., Zehavi, I. & Loveday, J. 2003, *AJ*, 125, 2276
- Brainerd, T. G. 2005, 628, L101
- Conroy, C., Gunn, J. E. & White, M. 2009, *ApJ*, 699, 486
- De Lucia, G., Springel, V., White, S. D. M., Croton, D., & Kauffmann, G. 2006, *MNRAS*, 366, 499
- De Lucia, G., & Blaizot, J. 2007 *MNRAS*, 375, 2
- Fukugita, M., Ichikawa, T., et al. 1996, *AJ*, 111, 1748

- Guo, Q., White, S., Li, C. & Boylan-Kolchin, M. 2010, MNRAS, 404, 1111
- Hogg, D.W., Schlegel, D.J. et al. 2001, AJ, 122, 2129
- Kauffmann G., Heckman, T. M., White, S. D. M., Charlot, S., Tremonti, C., Peng, E. W., Seibert, M., Brinkmann, J., Nichol, R. C., SubbaRao, M., & York, D. 2003, MNRAS, 341, 33
- Komatsu, E. et al. 2011, ApJS, 192, 18
- Li, C., Kauffmann, G., Wang, L., White, S. D. M., Heckman, T. M. & Jing, Y. P. 2006, MNRAS, 373, 457
- Lilliefors, H. W. 1969, JASA, 64, 387
- More, S., van den Bosch, F. C., Cacciato, M., Skibba, R., Mo, H. J. & Yang, X., 2011, MNRAS, 410, 210
- Navarro, J. F., Frenk, C. S., White, S. D. M., 1995, MNRAS, 275, 720
- Navarro, J. F., Frenk, C. S., White, S. D. M., 1996, ApJ, 462, 563
- Navarro, J. F., Frenk, C. S., White, S. D. M., 1997, ApJ, 490, 493
- Sales, L. & Lambas, D. G. 2004, MNRAS, 348, 1236
- Sales, L. & Lambas, D. G. 2009, MNRAS, 395, 1184
- Sales, L., Navarro, J. F., Lambas, D. G., White, S. D. M. & Croton, D. J. 2007, MNRAS, 382, 1901
- Salim, S. et al. 2007, ApJS, 173, 267
- Siverd, R., Ryden, B. & Gaudi, B. S. 2009, preprint, submitted to ApJ (arXiv:0903.2264)
- Smith, J. A., Tucker, D. L., Kent, S. M., et al. 2002, AJ, 123, 2121
- Springel, V., et al. 2005, Nature, 435, 629
- Strateva I., et al., 2001, ApJ, 122, 1861
- Strauss, M. A., Weinberg, D. H. et al. 2002, AJ, 124, 1810
- Weinmann, S. M., van den Bosch, F. C., Yang, X., & Mo, H. J., 2006, MNRAS, 366, 2
- York, D. G., Adelman, J., Anderson, J. E., et al. 2000, AJ, 120, 1579